

1
2
3
4
5
6
7
8
9
10
11
12
13
14
15
16
17
18
19
20
21
22
23
24
25

Numerical study of ice-induced loads and responses of a monopile-type offshore wind turbine in parked and operating conditions

Wei Shi^{a,b,*}, Xiang Tan^{a,b,d}, Zhen Gao^{a,b,c}, Torgeir Moan^{a,b,c}

^a *Department of Marine Technology, Norwegian University of Science and Technology (NTNU), Trondheim, Norway*

^b *Centre for Ships and Ocean Structures (CeSOS), NTNU, Trondheim, Norway*

^c *Centre for Autonomous Marine Operations and Systems(AMOS), NTNU, Trondheim, Norway*

^d *Multiconsult AS, Tromsø, Norway*

Corresponding Author: Wei Shi
TEL: +47 73595602
E-mail: shi.wei862@gmail.com

1 **Abstract**

2 Offshore wind is an attractive source of renewable energy. In regions with cold
3 climates, such as Canada, the Baltic Sea, and Bohai Bay, a good understanding of ice
4 loads is essential to design a reliable and cost effective support structure for an offshore
5 wind turbine. This paper presents a study of the dynamic ice-structure interaction of a
6 commonly used monopile-type offshore wind turbine in drifting level ice in both parked
7 and operating conditions. A semi-empirical numerical model for ice-structure
8 interaction was coupled to the aero-hydro-servo-elastic simulation tool HAWC2. A
9 convergence study was performed to determine the proper time step and simulation
10 length to obtain reliable response prediction. The simulated ice load was compared with
11 the formulations in international standards. The coupling between the ice loads and the
12 structural response of the monopile-type wind turbine was investigated and found to be
13 important. The effects of the ice characteristics (e.g., ice thickness and drifting speed)
14 were examined with the turbine being in parked and operating conditions. Compared
15 with current numerical model, standards from International Electrotechnical
16 Commission (IEC) and International Organization for Standardization (ISO) predict
17 lower ice loads. 3-D effect of ice-monopile interaction and failure of local ice sheet are
18 considered. More stochastic dynamic phenomena are captured for ice-structure
19 interaction in our numerical model. The effect of the ice thickness on the response was
20 found to be significant. A negligible drifting speed effect is found on the bending
21 moment response in the fore-aft direction. There is a large increase in the fore-aft
22 response as the inclination angle of the cone increases. Further sensitivity studies and
23 validation against model tests will be performed for the conical waterline of the wind
24 turbine.

1 *Keywords*

2 Offshore wind energy; Monopile; Numerical model; Ice-structure interaction; Coupled
3 simulation

4
5 **1. Introduction**

6
7 Offshore wind energy is recognized as one of the world's fastest growing renewable
8 energy resources. Deployment of wind turbine technology at offshore sites offers a
9 promising but challenging solution due to the severe environmental conditions imposed
10 by waves and currents. By the end of 2014, there was 8 GW of offshore wind energy
11 installed in Europe, including 2,488 turbines in 74 wind farms in 11 European countries
12 (Corbetta et al., 2015). Another 12 on-going projects will contribute an additional 3 GW
13 by 2016 according to the European Wind Energy Association (EWEA). Due to various
14 challenges in developing offshore wind technology, numerical modeling and the
15 automatic control of offshore wind turbines are currently being investigated intensively
16 (Perveen et al., 2014; Jiang et al., 2014; Karimirad and Moan, 2013; Shi et al. 2013).

17 Offshore wind turbines (OWTs) have significant potential in northern regions with
18 cold climates, such as Northern Asia, North America, and Northern Europe.
19 Approximately 20% of the European OWTs, which produce 10 GW in total, is to be
20 installed in the Baltic Sea by 2020 based on an EWEA forecast (Arapogianni and
21 Genach, 2013). Bottom-fixed wind turbines are very suitable in these offshore areas.
22 Besides the aerodynamic and hydrodynamic, ice loads would also be an important load
23 for OWTs in cold areas. The design standards for bridge, lighthouses, and oil and gas
24 platforms contain information about structural design against ice loads; however, those

1 standards and guidelines are not always suitable for the design of OWT support
2 structures due to the excessive dynamic effects that are typically present in the latter
3 type of structure. Therefore, the challenges related to ice loads on OWTs are not well
4 understood and have not been investigated in detail to date. Icing on OWT blades and
5 drifting-level-ice-induced ice loads are two different ways that ice can affect wind
6 turbines. Icing on OWT blades will increase the mass and thus change the aerodynamic
7 performance of WTs, leading to increased dynamic loads and reduced power production
8 (Etemaddar et al., 2014; Ronsten et al., 2012). Drifting ice could induce dynamic loads
9 and may cause failure in the support structures of OWTs. For a 5 MW OWT on a
10 monopile with diameter of 6 m interacting with drifting ice that has a thickness 0.5 m,
11 the ice-structure interaction could generate dynamic forces as high as maximum of 15
12 MN under conservative simplifications (Nguyen et al., 2014); this is far higher than the
13 wind thrust force of 0.8 MN for 5 MW wind turbine at 11.4 m/s turbulent wind. Ice
14 loads on the support structures for OWT in cold regions could add risks and increases
15 cost of construction and maintenance (Salo and Syri, 2014). These ice loads can thus be
16 of critical concern in the design of WTs; this calls for a detailed study of ice-induced
17 vibrations in OWTs.

18 For offshore structures used in oil and gas industry in cold regions, ice loads may be
19 dominant over wind and wave loads (Hou and Shao, 2014; McGovern and Bai, 2014).
20 Many studies have been conducted to predict the ice loads on cylindrical or sloped
21 offshore structures. Bekker et al. (2009) carried out simulations of the ice-structure
22 interaction between the ice cover and the offshore structures. Grtner et al. (2009)
23 simulated ice actions on Norstrmsgrund lighthouse by means of a finite element model
24 of the ice with the computational cohesive elements model. Zvyagin and Sazonov(2014)

1 used a probabilistic model to simulate the stochastic ice loads. Bekker et al. (2013)
2 estimated contact interaction of ice hummock and ice floe to predict the ice load on a
3 cylinder using commercial CFD-software. Spencer et al. (2014) used the quantile
4 regression method to analyze global ice pressure data for a wide range of structures.
5 Taylor and Richard (2014) developed a probabilistic ice load model based on empirical
6 method. Conical structures have been suggested for most offshore structures where ice
7 is present because they can induce bending failure in level ice by introducing a vertical
8 force component into the total interaction force using upward or downward cones (Xu et
9 al. 2014). The cone reduces the ice load magnitude and ice-induced structural response
10 compared to a cylindrical structure with the same waterline diameter (Barker et al.,
11 2014). A conical structure is also less likely to lead to severe dynamic ice load because
12 the period of bending failure in level ice, which depends on the ice thickness and the
13 drifting speed, is typically longer than that of crushing failure in level ice against a
14 vertical structure. Ralston's formula was adopted in IEC 61400-3 (2009) and DNV-OS-
15 J101 (2014) to calculate static ice loads on conical structures based on plastic limit
16 analysis. Several Design Load Cases are provided in IEC standard to consider both
17 parked and power production modes. Modern standards for ice load prediction of
18 offshore structures were reviewed by Frederking (2012). Popko et al. (2012a) studied
19 the sea ice loads on offshore support structures by comparing different ice models from
20 different guidelines and standards. They indicated that the interaction of sea ice, other
21 metocean loads and OWT should be considered.

22 Serious ice induced vibrations of offshore structures have been seen to occur in situ.
23 A limited number of campaigns measured ice loads and response in model tests and
24 field observations involving the ice-induced vibrations (Jefferies et al., 2011).

1 Määttänen et al. (2011) conducted near full-scale ice crushing tests in Aker Arctic test
2 basin. Frequency lock-in crushing may cause severe vibration at certain ice velocities
3 for cylindrical structures (Bjerkås et al. 2013; Bjerkås et al. 2014; Xu et al. 2014). It is
4 also important to determine the force and frequency of loads cycles for fatigue
5 assessment (Hendrikse et al., 2014). This phenomenon is specially addressed in ISO
6 (2010) and IEC standards (2010). Murray et al. (2009) did model tests in a scale of 1:30
7 and 1:50 to predict ice loads of an ice resistant spar design. Nord et al. (2015) identified
8 the force induced by level ice on a generic bottom-fixed offshore structure using a joint
9 input-state algorithm to describe experimental ice-induced vibrations. Zhou et al. (2012)
10 compared numerical simulations of ice breaking loads with the model tests in an ice
11 tank, where the ice loads were measured during the different ice drift speeds, ice
12 properties and ice drift angles. Full-scale testing was conducted by Yue et al. (2009) on
13 a cylindrical monopile in Bohai Bay to investigate the dynamic ice forces and structural
14 vibrations; three speed-dependent ice force modes were observed. Following their
15 previous work, Xu and Yue (2014) experimentally investigated the dynamic ice force
16 on a jacket structure with an upward ice-breaking cone in the Bohai Sea.

17 Several studies have been performed on relevant feature for OWT. When calculating
18 ice loads, the coupling effect due to WT aerodynamic loads is typically not considered
19 in most standards. The excitation of a complete OWT structure and the vibration of its
20 blades were reported by Heinonen et al. (2011) and Hetmanczyk et al. (2011) in a
21 numerical study of the dynamic ice loads on an OWT. Gravesen and Kärnä (2009)
22 focused on the static ice crushing occurring on a vertical structure of an OWT in the
23 South Baltic Sea based on the ISO standard (2010) with necessary corrections to the ice
24 reference strength. Barker et al. (2005) and Gravesen et al. (2003, 2005) performed an

1 extensive model testing to investigate the ice-induced vibrations in OWTs in Danish
2 waters. Mitigation of ice-induced vibrations in an OWT was studied using a semi-active
3 model (Mróz et al., 2008) and semi-active tuned mass damper (STMD) system (Kärnä
4 and Kolari, 2004). Yu et al. (2013, 2014) considered the floating ice cover as a rigid-
5 plastic structure supported by an elastic foundation. The quasi-static ice loads were
6 generated using relationship between ice force and displacement field of the ice using
7 the mode approximation method. They used both limit strain and limit strain rate as ice
8 breaking criteria. In their model, the contact between the ice and the structure is simply
9 assumed as a single point contact for three-dimensional application. Interaction between
10 the level ice and OWT considering structure motion and velocity were not included. No
11 detailed contact information between ice and OWT were included.

12 Wind turbine design and analysis rely on the use of aero-hydro-servo-elastic
13 simulation tools to predict the coupled dynamic loads and responses of an OWT;
14 however, limited amounts of research have considered fully coupled analyses, which
15 simultaneously investigate the effects of both aerodynamic and ice loads on the
16 behavior of offshore wind turbines.

17 As an extension of a previous study by Shi et al. (2014), this paper aims to develop
18 and implement a numerical semi-empirical ice load analysis method in the aero-hydro-
19 servo-elastic tool HAWC2 (Larsen and Hansen, 2014) to investigate the intricate
20 dynamic ice-structure interaction process for a monopile WT. The level ice load model
21 used in this study has been well validated for level ice and a circular platform (Su et al.,
22 2010; Zhou et al., 2012; Tan et al. 2013; Tan et al., 2014). An inverted ice-breaking
23 cone is added to the monopile at the mean sea level (MSL) to mitigate the ice loads on
24 the structure. Different from other ice models (Yu et al., 2013; Yu et al., 2014), the

1 proposed model uses the dynamic ice bending model to take into account the relative
2 motion and velocities between structures and ice such that the monopile response
3 influenced the interaction force between the cone and the ice. A series of icebreaking
4 events could be simulated and detailed contact information could be observed based on
5 the updated ice geometry. A dynamic link library (DLL) is used to feed the ice forces at
6 each time step into the HAWC2 based on the input position and velocity of the
7 monopile using an iterative procedure. Meanwhile, the instantaneous ice-breaking
8 pattern can be checked for the contact status between the cone and the ice. Especially,
9 the proposed ice load model, based on 3D contact model, makes it possible to estimate
10 the ice load in the Side-to-Side (S-S) direction, which may be of similar magnitude as
11 that in the Fore-After (F-A) direction. Particular efforts are made to study convergence
12 w.r.t. time step and simulation length. Coupled dynamic analyses are carried out to
13 study the effects of the ice parameters, such as ice drifting speed and ice thickness. The
14 simulated ice load from this study is then compared with the characteristic loads given
15 in design standards of IEC and DNV. The responses of the wind turbine under parked
16 and operating conditions are finally compared under different ice conditions.

17 In this model, the downward ice-breaking cone is attached to the monopile at the
18 MSL. The cone will reduce the ice loads by changing failure mode from crushing to
19 bending. However, due to increased waterline diameter, D_{wl} , the hydrodynamic loads
20 from wave and current may increase. For a wave condition at Gulf of Bothnia with 50-
21 year ice-time-included significant wave height of 8.123 m and wave peak period of 12.0
22 s (Tuomi et al., 2011), the estimated maximum wave load increases from 2273 kN to
23 2502 kN because of ice-breaking cone. The maximum ice load is 1908 kN for a level
24 ice thickness of 0.8 m and a drifting speed of 0.5 m/s. The crushing loads would be

1 5064 kN for this ice condition. This shows that ice-breaking cone will not give
2 significant increase of wave load at the Baltic Sea, which is also shown in Määttänen's
3 work (Määttänen, 1999).

4

5 **2. Numerical model**

6

7 *2.1 Ice-structure interaction model*

8 *2.1.1 Ice failure modes*

9 Due to differences in the ice thickness, the ice drifting speed and the geometry of the
10 structure, ice failure can be classified as (ISO 19906, 2010): crushing mode, which
11 typically occurs against vertical structures; and flexural mode, which typically occurs
12 against inclined structures. Depending on the ice speed, the crushing mode could be
13 identified as (Yue et al., 2009; ISO 19906, 2010):

14 1) Intermittent ice crushing at low ice velocities, where the ice-load time series
15 exhibit a saw-tooth waveform with a specified period that is separated by unloading
16 intervals;

17 2) Frequency lock-in crushing at moderate ice velocities, where the ice-load time
18 series exhibit a periodic waveform at a specified fundamental frequency (i.e., the natural
19 frequency of the motion or vibrations) of the support structure;

20 3) Continuous brittle crushing at high ice velocities, where the time series of both the
21 ice loads and the structural response appear to be random.

22 Conical structures are added to OWT towers at the mean sea level to mitigate the ice
23 loads by changing the failure modes from crushing to bending (Fig. 1) (Barker et al.,
24 2005). A vertical force is introduced into the total interaction force by these conical

1 structures, which triggers the flexural failure mode in the ice. When there is a relative
2 speed between the monopile circumference and the ice sheet, ice-structure contacts and
3 individual bending failure events of the ice sheet may occur at different positions of the
4 monopile circumference. In general, these failure events are nonsimultaneous, and each
5 is followed by a subsequent contact-bend event. Thus, when observing the ice-structure
6 interaction in the time domain, the failure of the ice sheet can be viewed as a
7 composition of successive bending failure events occurring at different location of
8 contact along the monopile circumference. In this study, only flexural failure is
9 considered for the ice-breaking cone; it is also assumed that ice drifts along the
10 downwind direction.

11

12 *2.1.2 Ice-breaking process*

13 In this section, mathematical modeling of the ice-breaking process is briefly
14 described. Detailed information about this process is described by Tan et al. (2013,
15 2014).

16 When an ice sheet is passing a wind turbine monopile, the ice-breaking cone comes
17 into contact the edge of the level ice. Local failure could occur at the loaded areas as the
18 ice sheet continues to move past the monopile. Some areas of the ice edges begin to fail
19 in bending when the vertical load exceeds the bearing capacity of the ice. Then, the
20 broken ice pieces continue to slide along the surface of the cone; this may lead to the
21 accumulation of ice rubble in front of the structure due to a poor ice clearing ability. In
22 this study, it is assumed that these ice pieces are well cleared after failure. The process
23 of the ice-structure interaction during flexural failure of the ice is illustrated in Fig. 2 for
24 detail (ISO 19906, 2010).

1 To solve the equations of motion (EOM) for the entire wind turbine system, the ice-
2 breaking force from the ice load model must be explicitly determined for each time step.
3 The ice breaking force was calculated by the contact algorithm developed in previous
4 work (Su et al., 2010; Tan et al., 2013, 2014). The dynamic displacements of the
5 structure at the MSL, which change the local slope angle of the structure, are considered
6 by numerically updating the waterline's geometry. The instantaneous waterline and an
7 auxiliary waterline below it are discretized into nodes and updated at each time step (Fig.
8 3). The ice is also discretized into nodes based on the initial condition or edge shape
9 from the previous time step. Contact panels are constructed between the two waterlines,
10 and overlaps between the water line and the ice edge are considered to be contact zones.
11 The contact area is calculated based on the indentation depth, slope angle and the ice
12 thickness. The local contact forces are shown in Fig. 4. The nodal velocity based on a
13 local coordinate system (τ, n, z) (Fig. 4(a)) can be decomposed into the tangential
14 component (v_1) and the normal component (v_2) to the contact surface in $(\tau, l, 2)$ (Fig.
15 4(c)):

$$16 \quad v_i^{(\tau,1,2)} = \begin{bmatrix} v_\tau \\ v_1 \\ v_2 \end{bmatrix} = \begin{bmatrix} 1 & 0 & 0 \\ 0 & \cos \varphi_i & \sin \varphi_i \\ 0 & \sin \varphi_i & -\cos \varphi_i \end{bmatrix} \begin{bmatrix} v_\tau \\ v_n \\ v_z \end{bmatrix} \quad (1)$$

17 The local normal crushing force (Fig. 4(b)), F_{cr} , is calculated based on the contact
18 area, A_{cr} , and the average crushing pressure, p_{av} (Riska, 1995):

$$19 \quad F_{cr} = \begin{cases} -p_{av} A_{cr}, & v_2 \leq 0 \\ 0, & v_2 > 0 \end{cases} \quad (2)$$

20 where the negative sign indicates that the force is always in the direction opposite to v_2 .

1 The contact area for each contact zone, A_{cr} , can be calculated based on the indentation
 2 depth, L_h , the inclination angle of the cone with the horizontal, φ , and ice thickness, h_i
 3 (Su et al., 2010):

$$4 \quad A_{cr} = \begin{cases} \frac{1}{2} L_h \frac{L_d}{\cos \varphi}, & L_d \tan \varphi \leq h_i \\ \frac{1}{2} \left(L_h + L_h \frac{L_d - \frac{h_i}{\cos \varphi}}{L_d} \right) \frac{h}{\sin \varphi}, & L_d \tan \varphi > h_i \end{cases} \quad (3)$$

5 The average contact pressure, p_{av} , depends on the magnitude of the contact area,
 6 which is known as the pressure-area relation:

$$7 \quad p_{av} = k A_{cr}^n \quad (4)$$

8 where k and n are empirical parameters.

9 On plane τ -1, the tangential friction force, f_l , and the horizontal friction force, f_t , can
 10 be calculated by decomposing the total friction force, f , respectively (Fig. 4(d)):

$$11 \quad f_l = \mu F_{cr} \frac{v_1}{\sqrt{v_\tau^2 + v_1^2}} \quad (5)$$

$$12 \quad f_\tau = \mu F_{cr} \frac{v_2}{\sqrt{v_\tau^2 + v_1^2}} \quad (6)$$

13 The nodal forces on the ice-breaking cone in (τ, n, z) can be obtained by

$$14 \quad F_i^{(\tau, n, z)} = \begin{bmatrix} F_\tau \\ F_n \\ F_z \end{bmatrix} = \begin{bmatrix} 1 & 0 & 0 \\ 0 & \cos \varphi_i & \sin \varphi_i \\ 0 & \sin \varphi_i & -\cos \varphi_i \end{bmatrix} \begin{bmatrix} f_\tau \\ f_l \\ F_{cr} \end{bmatrix} \quad (7)$$

15 Finally, the nodal forces in the local coordinate system can be transformed into the
 16 global coordinate system. The global ice load is obtained by integrating the local contact
 17 loads over all of the contact zones acting on the ice-breaking cone simultaneously.
 18 Detailed information about this process can be found in Tan's work (2013).

1

2 2.1.3 Bending failure criterion

3 The ice edges are loaded by the reaction forces from the ice cone. The vertical
4 reaction force, F'_z , which points downwards, includes two components: the normal
5 crushing force F_{cr} and the tangential friction force f_1 :

$$6 \quad F'_z = -F_z = -(F_{cr} \cos \varphi - f_1 \sin \varphi) \quad (8)$$

7 By substituting Eqs. (2), (5), (7) into (8), we find:

$$8 \quad F'_z = \left(\cos \varphi - \mu \frac{v_n \sin \varphi \cos \varphi + v_z \sin^2 \varphi}{\sqrt{v_\tau^2 + (v_n \cos \varphi + v_z \sin \varphi)^2}} \right) p_{av} A_{cr} \quad (9)$$

9 where p_{av} and A_{cr} can be found using Eqs. (3) and (4).

10 As the level ice impacts the monopile and continues to move past the monopile, the
11 contact area and the force between the ice and cone increase. When the vertical force,
12 F'_z (Eq. 9), exceeds the dynamic bending failure load, P_f , of the ice edge, bending
13 failure occurs in the ice. Once the broken ice splits from the ice sheet, a new ice edge is
14 formed, and the next ice-structure contact cycle begins. The ice-breaking pattern
15 induced by continuous ice-structure interaction is shown in Fig. 6.

16 The bending failure load, P_f , is determined based on a semi-empirical relation (Eq.10)
17 (Tan et al., 2014):

$$18 \quad P_f = (1.65 + 2.47v_2^{0.4}) \sigma_f h_i^2 \left(\frac{\theta_w}{\pi} \right)^2 \quad (10)$$

19 where, v_2 is the normal relative speed, σ_f is the bending strength, $\left(\frac{\theta_w}{\pi} \right)^2$ is the geometry
20 factor specifying the wedge size in the circumferential dimension.

1 Yu et. al (2013, 2014) use both limit strain and limit strain rate as ice breaking criteria.
 2 The ice-breaking length should be calculated first from the limit strain rate or the limit
 3 strain of the ice, which should be given for each case. In general, these two limit values
 4 are hard to find. From their model, bending failure force can be expressed as (Eq.11):

$$5 \quad P_f = 2\sqrt{2}\sigma_f h_i^2 \quad (11)$$

6 Compared with Eq. 10, it shows that loading rate effect and structure motions (term
 7 including v_2) are not taken into account. Meanwhile, the ice wedge geometry $\left(\frac{\theta_w}{\pi}\right)^2$ is
 8 not considered, which means the detailed contact information between ice and structure
 9 cannot be observed.

10 Our numerical model considered the 3D effect of the ice-monopile interaction.
 11 Because the monopile has a large diameter relative to the size of broken ice sheet, the
 12 ice sheet will have different contact points along the circumference of the monopile and
 13 fail at different locations. This induces a dynamic effect on the total ice loading, which
 14 is not captured by the models in IEC and ISO standards. In IEC 61400-3 (2009),
 15 Ralston's formulae, which has also been used as recommended practice in DNV and
 16 API standards, is adopted to calculate the static ice loads on conical structures, For
 17 downward breaking cones, the static characteristic value for horizontal and vertical
 18 forces on the cone are:

$$19 \quad F_H = A_4 \left(A_1 \sigma_f h_i^2 + \frac{1}{9} A_2 \rho_w g h_i D_{wl}^2 + \frac{1}{9} A_3 \rho_w g h_i (D_{wl}^2 - D^2) \right) \quad (12)$$

$$20 \quad F_V = B_1 F_H + \frac{1}{9} B_2 \rho_w g h_i (D_{wl}^2 - D^2) \quad (13)$$

1 where A_i and B_i are non-dimensional coefficients determined from the reference
2 (Ralston, 1977). ρ_w is the water density, D is the cone diameter at the bottom for
3 downward cone.

4 For dynamic loading on conical structures, IEC recommends the following vertically
5 shifted sinusoidal model as:

$$6 \quad F_{H,dyn} = F_H \left(\frac{3}{4} + \frac{1}{4} \sin(2\pi f_b t) \right) \quad (14)$$

7 where F_H is the maximum load derived from static characteristic value (Eq. 12), and
8 $f_b = V_i / (Kh_i)$, V_i is the ice drifting speed, h_i is the ice thickness, and $4 < K < 7$, the value K
9 which gives the highest load should be used.

10 IEC also suggests sawtooth model for dynamic loading on conical structures as in Fig.
11 7. The characteristic values in the IEC static model, periodical IEC sin dynamic model
12 and IEC sawtooth dynamic model are the maximum ice loads, which are the same as
13 IEC static model (Eq. 12).

14

15 *2.2 Coupled aero-hydro-servo-elastic analysis*

16 In this study, numerical simulations were performed using HAWC2, which was
17 developed at the Technical University of Denmark (DTU) (Larsen and Hansen, 2014).
18 The HAWC2 code is used to perform the fully coupled aero-hydro-servo-elastic
19 analyses for wind turbine systems; its features have also been verified in IEA OC3 and
20 OC4 benchmarks (Jonkman et al., 2010; Popko et al., 2012b; Robertson et al., 2014).
21 HAWC2 can effectively simulate the dynamic response of a pitch-controlled horizontal-
22 axis wind turbine that is subjected to aerodynamic and hydrodynamic loads. The FAST
23 code is based on modal theory, which gives linear structural response. It uses a

1 combined linear FEM with beam elements and a nonlinear MBS formulation to
2 calculate the structural dynamics of the wind turbine in the time domain. Therefore, the
3 code is particularly suited to calculate the loads in flexible turbines with large
4 deflections and rotations. In FAST, The aerodynamic forces on the rotor are calculated
5 in the HAWC2 using Blade Element Momentum (BEM) theory. The classic approach
6 has been modified to include the effects of dynamic inflow, dynamic stall, skewed
7 inflow, shear effects on induction and the effects from large deflections. The
8 hydrodynamic loads in the HAWC2 are calculated based on the well-known Morison's
9 equation. Both regular and irregular Airy waves could be used by defining the wave
10 kinematics externally through a dynamic link library (DLL). The interaction between
11 the foundation and the soil is modeled by a p - y curve with a set of spring-dampers
12 attached to the main body based on the API standard (API, 2007). Control of the turbine
13 (e.g., pitch control, yaw control) is performed through one or more DLLs. Any external
14 force, such as ice loads, slamming force, ship impact force, can be applied to the
15 structure using these DLLs.

16 In this study, the ice-structure interaction model described in Section 2.1.2 is
17 implemented into HAWC2 as a user-defined external force via a DLL generated in
18 FORTRAN. The continuous icebreaking process is discretized into successive time
19 steps. Due to the coupling of the ice forces and the structure motion, iterations are
20 performed to get dynamic equilibrium at each temporal integration point. At each
21 iteration, the ice-breaking forces are calculated according to the current state variables
22 of the cone, the current ice edge shape and the cone-ice contact geometry. Then, the
23 calculated ice 6-DOF ice-load vector is transferred back to the node at the mean sea
24 level in HAWC2 to solve the equations of motion of the whole wind turbine system for

1 the current iteration (Fig. 8). The incremental displacements are found. The state
2 variables of the cone are updated by the vector sum of the increments and the initial
3 values at the beginning of the time step. According to the indentation of the cone edge
4 into the ice, local contact speed, and material properties of the ice, a new ice edge is
5 generated. In the coupled analysis, the dynamic deformation of the monopile is
6 considered during contact detection, which is neglected in the uncoupled analysis (Shi
7 et al., 2014).

8

9 **3. Simulation results**

10

11 *3.1 Wind turbine and ice properties*

12 *3.1.1 Wind turbine properties*

13 The wind turbine model chosen for this study is the National Renewable Energy
14 Laboratory (NREL) 5-MW baseline WT. Overall, the NREL 5-MW turbine is a
15 conventional, three-bladed, upwind, variable-speed and collective-pitch-controlled
16 horizontal-axis wind turbine (HAWT). Its main properties are listed in Table 1
17 (Jonkman et al., 2009). Its diameter and wall thicknesses vary linearly with the tower
18 height. The tower base diameter is equal to the diameter of the monopile, which is 6 m.
19 A water depth of 20 m is considered in this study. The pile below the mudline was
20 assumed to be rigid. The ice-breaking cone used in this study is a 45°-inverted cone with
21 waterline width of 8 m (Fig. 1) that is rigidly attached to the monopile at the MSL. No
22 deformation in the cone is considered.

23

24 Table 1. Main characteristics of the NREL 5-M baseline OWT.

Parameter	Value
Rated power	5 MW
Rotor Orientation	Upwind
Rotor/Hub Diameter	126 m, 3 m
Cut-In, Rated, Cut-Out Wind Speed	3 m/s, 11.4 m/s, 25 m/s
Cut-In, Rated Rotor/ Generator Speed	6.9 rpm, 12.1 rpm/ 670 rpm, 1,173.7 rpm
Overhang, Shaft Tilt, Precone	5 m, 5°, 2.5°
Rotor, Nacelle, Tower Mass	110 t, 240 t, 347.46 t
Tower top diameter, wall thickness	3.87 m, 0.019 m
Pile length above seabed, diameter	30 m, 6 m
Pile wall thickness, total weight	0.06 m, 187.9 t

1

2 3.1.2 Ice properties

3 The representative ice properties suggested by the ISO standard for Baltic Sea are
4 listed in Table 2 (ISO 19906, 2010).

5 Table 2. Ice properties.

Parameter	Symbol	Value
Density	ρ_{ice}	880 kg/m ³
Crushing strength	σ_c	2.3 MPa
Bending strength	σ_f	580 kPa
Young's Modulus	E	5.4 GPa
Poisson ratio	ν	0.33
Coefficient of friction	μ	0.05
Ice sheet thickness	h_i	0.1 m~0.8 m
Ice drifting speed	V_i	0.1 m/s~0.5 m/s

6

1

2 3.2 Ice-load effects on the dynamic response of OWTs

3 3.2.1 Characteristics of the wind turbine system

4 The natural frequencies and natural modes of the monopile supported wind turbine
5 are determined using the eigen frequency analysis in the HAWC2. The modes and
6 corresponding natural frequencies relating to the wind turbine tower are shown in Table
7 3. Other modes and frequencies related to blade vibrations are not shown here.

8 Table 3. Natural frequencies and mode shapes relating to the OWT tower modes.

Full System Eigenmode	Natural Frequency (Hz)
1st Tower F-A	0.274
1st Tower S-S	0.276
2nd Tower F-A	2.284
2nd Tower S-S	2.278

9

10 3.2.2 Ice-induced dynamic response of OWTs

11 In this section, we investigate the influence of the ice load on the dynamic response
12 of the wind turbine under different load cases (Table 4). In LC1.1, a rigid wind turbine
13 model is considered in the parked condition with a zero wind speed; a level ice field
14 with a drifting velocity, V_i , of 0.5 m/s and an ice sheet thickness, h_i , of 0.4 m is assumed
15 in this case. In LC1.2, a flexible wind turbine in the parked condition with the same ice
16 conditions is assumed. In LC1.3, a flexible wind turbine is operated at the rated wind
17 speed (wind speed, $V_{wind} = 11.4$ m/s), but no ice is present. In LC1.4, a flexible wind
18 turbine model is considered using the same ice field in LC1.1 case one.

19 Table 4. Load cases (LCs) used to investigate the effect of the ice-induced dynamic
20 response.

LCs	V_{wind} (m/s)	V_i (m/s)	h_i (m)	OWT Description
1.1	0	0.5	0.4	Rigid
1.2	0	0.5	0.4	Flexible
1.3	11.4	0	0	Flexible
1.4	11.4	0.5	0.4	Flexible

1

2 Fig. 9 shows an external ice load acting in the F-A direction at the MSL under
3 different load cases. The crushing force acting on the vertical structure with same
4 waterline diameter (Gravesen and Kärnä, 2009) and the ice-induced upper bound static
5 load acting on the conical structure (IEC 61400-3, 2009) based on Ralston's formula
6 (Ralston, 1977) are also compared. Two different dynamic models from the IEC
7 standard are also used to determine the loads of the moving ice on the conical support
8 structures (IEC 61400-3, 2009). In our numerical model, the 3D effect of ice-monopile
9 interaction and failure of local ice sheet are considered, which induces a dynamic effect
10 of ice loading. The numerical results give a stochastic behavior of the ice loading
11 depending on the initial contact condition between the ice sheet and the monopile
12 circumference at the MSL. Randomness in ice property, ice thickness and drifting speed
13 is not considered in this work. The IEC and ISO formulae are based on the assumption
14 that the simultaneous failure of the ice sheet occur at the contact area, a 2D
15 consideration. They are based on prescribed, periodical ice load model.

16 In case of 0.5 m/s and 0.4 m ice condition, the crushing force (3369 kN) on a vertical
17 cylinder with the same diameter as the cone at the MSL (8 m) is much larger than the
18 ice-induced loads on the conical structures. The static model predicts an upper bound
19 ice force (175.62 kN), which is far less than the maximum value estimated from the
20 model proposed in this study (Fig. 10). The dynamic sine and sawtooth models yield

1 marginally higher mean forces. However, the load frequency of the IEC dynamic
2 models is much smaller than that of the proposed model. This will affect the fatigue
3 damage accumulation of wind turbine. Due to the motion of the flexible structure, less
4 ice load is generated for the load cases with a flexible turbine in operating condition. In
5 the proposed model, three main phases including loading, unloading and zero stable
6 force are clearly identified in the ice-force time history. This feature has also been
7 observed in full-scale measurements (Xu and Yue, 2014).

8 Fig. 11 shows the response of the F-A shear force at the MSL under different load
9 cases. For the rigid body model, the shear response is the same as the external ice load
10 that is shown Fig. 9, which proves the correctness of the model. The responses from the
11 IEC dynamic sine and sawtooth models, which are based on the wind turbine base
12 structural frequency, have a long-period of oscillation, which may underestimate the
13 loads during a fatigue analysis. During normal operation condition with a wind speed of
14 11.4 m/s and the ice with the specific condition (0.5 m/s drifting speed and 0.4 m
15 thickness), the wind loads are shown to dominate the response with large mean value
16 and small standard deviation; however, the average shear force at the MSL increases by
17 12% due to the ice load. Especially, the variation for LC 1.4 considering constant wind
18 and ice is much larger than the variation for LC 1.3 which only considers the constant
19 wind. This may significantly affect the fatigue damage of the monopile.

20 In Fig. 12, the turbine response is compared under different load conditions. The solid
21 and dotted line represent the responses under ice or wind loads separately. The dashed
22 line is the superposition of the responses of the ice and wind loads, which is referred to
23 as the “uncoupled ice + wind” case. In the coupled analysis, the standard deviation of

1 the response is less than the “uncoupled ice + wind” case due to the motion induced by
 2 wind load, which may have different fatigue damage accumulation.

3

4 3.2.3 Convergence study of ice loads

5 In this section, convergence tests with respect to time step, Δt , and simulation length,
 6 T_{total} , are performed to ensure that the proposed numerical method can produce a
 7 convergent solution of the ice loads and induced responses.

8 Different time steps (0.01, 0.005, 0.002, 0.001, 0.0005 s) and simulation lengths (600,
 9 1200, 1800 s) are investigated. The F-A and S-S bending moments at the mudline are
 10 also illustrated in Table 5 and 6 as functions of the time step and the simulation length,
 11 respectively.

12 Table 5. Statistic results of the bending moment at the mudline and computational time
 13 as a function of time step. $h_i = 0.4\text{m}$, $V_i = 0.5\text{ m/s}$, $T_{total} = 1200\text{ s}$.

Time step (s)	Computational time (h)	Mean (kNm)		Std (kNm)	
		F-A	S-S	F-A	S-S
0.0005	29	189	32	3888	3206
0.002	24	186	24	3721	3300
0.001	16	206	40	3625	3022
0.002	5	214	13	3593	3010
0.01	3	659	119	3797	3896

14

15 Table 6. Statistic results of the bending moment at the mudline as a function of
 16 simulation length. $h_i = 0.4\text{ m}$, $V_i = 0.5\text{ m/s}$, $\Delta t = 0.001\text{ s}$.

Simulation length (s)	Mean (kNm)		Std (kNm)	
	F-A	S-S	F-A	S-S

600	206	40	3625	3022
1200	173	34	3847	3154
1800	174	3	3829	3073

1

2 As shown in Table 5 for a 1200-s simulation time, the computation time increases as
3 the time step decreases. To balance the computation time and the convergence of the
4 results, a time step of 0.001 s and a simulation time of 1200 s are finally selected for use
5 in these simulations.

6

7 3.2.4 Effect of the ice thickness

8 The influence of the ice thickness on the dynamic response of the wind turbine was
9 studied in this section. Both the parked condition and normal operating condition were
10 considered (Table 7). An ice field with a constant drifting speed of 0.3 m/s and an ice
11 thickness of 0.1, 0.4, and 0.8 m was considered in the following simulations. This ice
12 thickness range was suggested by the ISO standard for Baltic Sea (ISO19906, 2010).

13

14 Table 7. LCs and statistic results of the wind turbine response with different ice
15 thicknesses. $V_i = 0.3$ m/s.

LCs	V_{wind} (m/s)	h_i (m)	Mean(kNm)		Std(kNm)		Max(kNm)		
			F-A	S-S	F-A	S-S	F-A	S-S	
2.1a	0	0.1	-1274	1	268	310	3	1257	
2.1	2.1b	0	0.4	-50	390	1855	2084	6758	7966
	2.1c	0	0.8	4676	12	9823	5490	37694	25471
	2.2a	18	0	38718	4734	510	212	39726	5177
2.2	2.2b	18	0.1	38925	4737	557	359	40498	6201
	2.2b	18	0.4	40181	4779	2004	2665	49514	16862
	2.2d	18	0.8	44870	4732	8924	5354	75836	31491

1
2
3
4
5
6
7
8
9
10
11
12
13
14
15
16
17
18
19
20
21
22
23

Fig. 13 shows a 100-s time history of the calculated ice loads at the MSL in the F-A and S-S directions for ice thickness 0.1 m, 0.4 m and 0.8m. These ice loads were generated for the parked condition (wind speed = 0). The simulated ice force clearly shows loading, unloading and zero stable force phases. It is observed that in the case of 0.1 m-thick ice, the loading history is random (Fig. 13(a)); while in 0.4 m and 0.8 m - thick ice, the curves have a clear, regular, periodic saw-tooth-like pattern, with the load dropping to zero or to near zero between peaks (Fig. 13(b)-(c)). For the ice thickness of 0.1 m, non-simultaneous failure is dominant, and the breaking force continuously increases for several seconds before it drops. There are more local contact regions between ice edge and the cone. For the ice thickness of 0.4 m and 0.8 m, the ice fails simultaneously and the ice force drops before subsequently increasing. Different from other models in IEC or ISO standard, the current numerical model is based on 3D contact algorithm so that we could also calculate the ice loads in the S-S direction. Due to the symmetry of the ice cone, the ice load in the S-S direction oscillates about zero (Fig. 13(b)). The corresponding spectra of the simulated ice loads (Fig. 13) are shown in Fig. 14. In the case of 0.1 m-thick ice, the dominant ice-breaking frequency is at 1.58 Hz; while in the case of the ice thickness of 0.4 m and 0.8 m, there are multiple ice-breaking events at the waterline with the dominant ice-breaking frequency between 0.15 Hz and 0.6 Hz (Fig. 14(a)). For ice load in the S-S direction (Fig. 14(b)), there is no clear dominated breaking frequency in the case of 0.1 m-thick ice due to the non-simultaneous failure. For ice thickness of 0.4 m, the ice load is dominated by frequency of 0.2 Hz.

1 The statistical properties of the wind turbine F-A bending moment at the mudline as a
2 function of the ice thickness under both parked and operating conditions are shown in
3 Table 7. Under the parked condition, both the mean and standard deviation of the
4 bending moment increase significantly as the ice thickness increases. Under operating
5 condition, there is relatively little change (less than 4%) in the response at smaller
6 thicknesses (e.g., 0.1 m and 0.4 m) compared to the no-ice condition; this is because the
7 wind load dominates the response of the OWT compared to the ice during operating
8 condition. However, a large increase in the OWT response (approximately 15%) is
9 shown at the larger thickness (0.8 m).

10 The spectra of the wind turbine F-A bending moment at the mudline are shown in Fig.
11 15. In parked condition (Fig. 15(a)), the second tower bending frequency is clearly
12 shown in the responses for all different ice thicknesses. In case of 0.1 m-thick ice, first
13 tower bending frequency is also identified; while ice-breaking frequencies are clearly
14 shown in the case of 0.4 m and 0.8 m –thick ice. In operating condition with wind speed
15 of 18 m/s (Fig. 15 (b)), first tower bending frequency is strongly dominant of the F-A
16 bending moment response in case of 0.4 m-thick ice; ice-breaking frequency is the main
17 excitation resource in case of 0.8 m ice thickness. Comparing the F-A bending moment
18 under parked and operating conditions with the same ice conditions (e.g. ice drift speed
19 0.3 m/s, ice thickness 0.1m), there is a reduction of the response at the first and second
20 tower bending frequency due to the aerodynamic damping from rotating rotor.

21 The statistical properties of the wind turbine S-S bending moment at the mudline as a
22 function of the ice thickness under both parked and operating conditions are shown in
23 Table 7. In parked condition, the vibration variation increases dramatically as ice
24 thickness increases. In operating conditions, there is small effect on the mean value of

1 S-S bending moment due to ice loads because the mean value is dominated by the wind
 2 loads. However large increase of standard deviation of the response is induced by ice
 3 loads. This will increase the fatigue damage accumulation.

4 Fig. 16 gives the spectra of the wind turbine S-S bending moment at the mudline. In
 5 parked condition (Fig. 16 (a)), the first and second tower bending frequencies are
 6 clearly shown with ice thickness of 0.1 m; in case of 0.4 m-thick ice, the ice breaking
 7 frequency dominates the bending response and the second tower bending frequency is
 8 also visible; in case of 0.8 m-thick ice, the S-S bending moment is dominated by second
 9 tower bending frequency. In operating conditions (Fig. 16 (b)), the tower bending
 10 frequencies are clearly shown in the case of ice thickness of 0.1 m; with 0.4 m-thick ice,
 11 first tower bending frequency is the main excitation source; the responses are dominated
 12 by second tower bending frequency with the largest ice thickness of 0.8 m.

13

14 3.2.4 Effect of the ice drifting speed

15 The influence of the ice drifting speed on the dynamic response of the wind turbine
 16 was studied in this section. An ice field with a constant thickness of 0.4 m with an ice
 17 drifting speed of 0.1, 0.3, and 0.5 m/s was considered under both parked and operating
 18 conditions (Table 8). This ice drifting speed range was suggested by the ISO standard
 19 for Baltic Sea (ISO19906, 2010).

20

21 Table 8. LCs and statistic results of the responses with different ice drifting speeds.

22 $h_i = 0.4$ m.

LCs		V_{wind} (m/s)	V_i (m/s)	Mean(kNm)		Std(kNm)		Max(kNm)	
				F-A	S-S	F-A	S-S	F-A	S-S
3.1	3.1a	0	0.1	-114	-17	2411	310	7527	9223

	3.1b	0	0.3	-50	390	1855	2084	6758	8053
	3.1c	0	0.5	183	8	3759	3662	13426	12976
	3.2a	18	0	38718	4734	510	212	39740	5295
3.2	3.2b	18	0.1	40114	4730	1532	1829	47272	12958
	3.2b	18	0.3	40181	4779	2004	2665	49514	16862
	3.2d	18	0.5	40364	4736	2443	2991	49710	16404

1

2 A 100-s time history of the calculated ice loads at the MSL in the F-A and S-S
3 directions with different ice thicknesses is shown in Fig. 17. In our model, a dynamic
4 bending failure load, P_f (Eq.10), which was deducted to take into account the loading
5 rate effect arising from the ice wedge-water interaction (Tan et al., 2014), was used. The
6 inertial effect of the ice wedge may cause ventilation phenomena (Lu et al, 2012). There
7 is no significant increase in the mean ice loads with the different drifting speeds
8 investigated in this work for Baltic Sea; however, a significant change in the ice-
9 breaking period due to the different drifting speeds is evident. This is because ice-
10 breaking period is inversely proportional to the ice drifting speed assuming constant ice
11 breaking length. There is also a shift in the energy content from lower to higher
12 frequencies in the spectra of the simulated ice loads at the MSL as ice drifting speed
13 increases (Fig. 18).

14 Table 8 shows the statistical results of the wind turbine F-A bending moment at the
15 mudline as a function of the ice drifting speed under both parked and operating
16 conditions. In parked condition, there is a small increase in the turbine response;
17 however, a negligible drifting speed effect is found in operating conditions with ice
18 drifting speed from 0.1 m/s to 0.5 m/s. Fig. 19 shows the spectra of the wind turbine F-
19 A bending moment at the mudline at different ice drifting speeds. In most cases, second
20 tower bending frequency gives a rise to the F-A bending moment response. Ice breaking

1 frequencies can be identified at 3 m/s ice drifting speed under parked condition (Fig. 19
2 (a)). In operating conditions with wind speed of 18 m/s (Fig. 19(b)), the responses are
3 dominated by the first tower bending frequency at ice drifting speed of 0.1 m/s and 0.3
4 m/s and by the second tower bending frequency at ice drifting speed of 0.5 m/s. Due to
5 the aerodynamic damping, the F-A responses at the first and second tower frequencies
6 under operating condition (wind speed of 18 m/s) are damped compared with the
7 responses under parked condition.

8 Table 8 compares the S-S bending moments at the mudline with different ice drifting
9 speed in parked and operating conditions. For all the operating condition LCs with
10 different wind speeds, the drifting speed has marginal effect on the mean values of the
11 response. The standard deviation gradually increases as drifting speed increases. Largest
12 increase can be found at 5 m/s drifting speed in both parked and operating conditions.
13 Large effect of ice loads on the standard deviation of the S-S bending moment response
14 will affect the fatigue damage.

15 The spectra of the S-S bending moment at the mudline with different ice drifting
16 speeds show a similar energy content as F-A response. Under the parked condition, the
17 response is dominated by the first tower bending mode except the load case with 0.3 m/s
18 ice drifting speed, where the ice breaking frequency is dominant. With wind speeds of
19 18 m/s, the responses show a larger magnitude at first tower mode and second tower
20 mode.

21

22 *3.2.5 Effect of the geometry of ice-breaking cone*

23 A parameter study was carried out to investigate the effect of different the inclination
24 angle of the cone, (i.e., φ in Fig. 4: 45°, 65°, 80°). The waterline diameter was kept at 8

1 m to guarantee the same contact panel area. The simulated ice loads in the horizontal
 2 direction are compared in Fig. 20. The ice load was found to be much higher for the 80°
 3 cone where the ice interacted with a conical structure that was closest to 90°. Due to the
 4 large inclination angle, the time series of the ice is continuously crushed rather than fail
 5 in bending; the corresponding loads are generally very large compared to bending
 6 failure mode loads and the forces always remain above zero (Barker et al., 2005).
 7 Further sensitivity study will be carried out to find the limit of the inclination angle,
 8 below which the bending failure is dominant.

9 As shown in Table 9, there is a large increase in the mean and standard deviation of
 10 the F-A response as the inclination angle of the cone increases. Typically an 80° cone
 11 yields a much larger response in the OWT structure. Significant changes in the standard
 12 deviation of the S-S bending moment were also identified.

13 Table 9. Statistical properties of the bending moments at the mudline at different
 14 inclination angle of the cone. $h_i = 0.4$ m, $V_i = 0.5$ m/s, $V_{wind} = 0$ m/s, $D_{wl} = 8$ m.

Inclination angle	Mean(kNm)		Std(kNm)		Max(kNm)	
	F-A	S-S	F-A	S-S	F-A	S-S
45°	183	8	3759	3662	13426	12976
65°	2197	-49	7865	6002	29525	32888
80°	16441	283	12009	14625	58478	51807

15

16 4. Conclusions

17

18 In this study, a semi-empirical ice load model was implemented in the HAWC2 code
 19 using a coupled aero-hydro-servo-elastic time-domain simulation to investigate the
 20 influence of ice loads on a monopile-type offshore wind turbine with a downward ice-

1 breaking cone. The ice model used in this study has been validated in previous studies
2 for ships and a large cylindrical platform. A convergence study was performed to
3 determine the proper time step and simulation length to obtain reliable response
4 prediction. Coupled analyses were carried out considering wind loads and ice loads
5 simultaneously. The results were compared to those from uncoupled analyses to
6 investigate the importance of performing a coupled analysis. Only constant wind speed,
7 uniform ice thickness and drifting speed are considered. Moreover, the effect of
8 different ice properties and ice breaking cone geometry on the structural behavior of
9 OWTs was investigated.

10 The main conclusions are as follows:

11 (1) Proposed numerical model can capture more dynamic effect of ice loading
12 considering 3D effect of ice-monopile interaction and failure of load ice sheet.

13 Based on the detailed local contact states, such as the ice edge geometries,
14 the local contact speed, the local slope angle of the structure, et al, our numerical
15 model consider the 3D effect of ice-monopile interaction and failure of local ice
16 sheet, which induces a dynamic effect of ice loading. Such loading is also
17 stochastic depending on the initial contact condition between the ice sheet and the
18 monopile circumference at MSL. However, the ISO 19906 and IEC 61400-3
19 standards formulae are based on the assumption that the simultaneous failure of
20 the ice sheet occur at the contact area with a prescribed ice load models. They are
21 2D models with less dynamic properties. Compared to the ice loads models from
22 the IEC and ISO standards, the current model predicts a much larger maximum
23 ice loads but with shorter time between peaks in the cyclic ice loads. More
24 dynamic phenomena are captured for ice-structure interaction from our numerical

1 model. This will affect the fatigue damage accumulation in the wind turbine. The
2 ice loads in S-S direction can also be simulated from the proposed model which
3 is not predicted by the ice load models from these standards. The S-S loads may
4 cause the S-S response in the same order of magnitude as the F-A response for a
5 structure with a large diameter.

6 (2) Ice loads can introduce significant vibrations in the structure.

7 The ice loads produced by level ice moving at a constant drifting speed and
8 with a constant thickness were considered and compared to wind loads produced
9 by constant wind speeds. This study shows that the mean wind loads are larger
10 than the mean ice loads for the wind and ice conditions considered at Baltic Sea
11 (thickness of 0.4 m and speed of 0.5 m/s). However, the shear force response at
12 the MSL will increase 12% due to ice loads with the specific condition (0.5 m/s
13 drifting speed and 0.4 m thickness) compared with the only wind loads case (11.4
14 m/s).

15 (3) The thickness of ice has a significant effect on the response of OWT.

16 For the ice thickness range investigated in this paper for the Baltic Sea (0.1
17 m-0.8 m), the ice loads in the F-A direction increase significantly as the ice
18 thickness increases. In case of 0.1 m-thick ice, the loading history is more
19 random; in case of 0.4 m and 0.8 m-thick ice, the ice loads have a clear, regular,
20 periodic saw-tooth-like pattern. This is because both non-simultaneous and
21 simultaneous bending failures occur with 0.1 m-thick ice. The thickness of ice
22 has more significant effect on the S-S bending moment response compared with
23 the F-A response. The ice breaking frequencies were shown to dominate the
24 OWT F-A bending moment response at larger thickness (0.4 m and 0.8 m). The

1 first- and second- order tower frequencies were clearly identified in the S-S
2 bending moment response.

3 (4) The effect of the drifting speed of ice is negligible on the response of OWT.

4 For the ice drifting speed range investigated in this paper for the Baltic Sea
5 (0.1 m/s-0.5 m/s), there is no large difference in the ice loads in the F-A direction
6 as the ice drifting speed increases. A negligible drifting speed effect is found on
7 the bending moment response in the F-A direction. But there is a significant
8 change in the ice-breaking frequency. The variation of the S-S resonant response
9 increases significantly as the drifting speed increases. First tower bending
10 frequency dominates the bending moment response in S-S direction.

11 (5) The responses of OWT will increase as the inclination angle of cone increases.

12 There is a large increase in the mean and standard deviation of the F-A
13 response as the inclination angle of the cone increases. Ice-breaking cone can
14 reduce the ice loads significantly by changing the failure mode from crushing to
15 bending. However, wave loads will increase due to the larger waterline diameter
16 compared with the cylindrical monopile. For a wave condition at Gulf of Bothnia
17 with 50-year ice-time-included H_s of 8.123 m and T_p of 12.0 s, the estimated
18 maximum wave load increases from 2273 kN for a conical structure to 2502 kN
19 for a vertical cylinder. This value is comparable to the maximum ice load under
20 conditions in Baltic Sea (e.g. 0.8 m-thick ice with drifting speed of 0.5 m/s).

21 Further optimization of cone geometry is necessary to compensate the increased
22 wave loads according to local joint metocean conditions of wind, wave and ice.

23 The values for the empirical parameters in the ice load model used in this study are
24 based on experiences from ice load on ships. Further sensitivity studies and validation

1 against model tests will be performed for the conical waterline of the wind turbine. The
2 influence of the ice load on the fatigue of the offshore wind turbine will also be
3 investigated.

4

5 **Acknowledgements**

6

7 The authors would like to gratefully acknowledge the financial support of the
8 Research Council of Norway through the Center for Ships and Offshore Structures
9 (CeSOS) and the Centre for Autonomous Marine Operations and Systems (AMOS) at
10 the Norwegian University of Science and Technology (NTNU). The authors appreciate
11 the assistance provided by Torben J. Larsen, Anders Yde, and Anders M. Hansen from
12 DTU wind energy (Risø campus) in connection with the HAWC2 simulation.

13

14 **References**

15

16 API, American Petroleum Institute, 2007. Recommended Practice for Planning,
17 Designing and Constructing Fixed Offshore Platforms Working Stress Design.
18 Thomson Reuters, 21st Ed.

19 Arapogianni, A., Genach, A.B., 2013. Deep water—the next step for offshore wind
20 energy. European Wind Energy Association (EWEA).

21 Barker, A., Sudom, D., Sayed, M., 2014. Conical structures in ice: The roles friction
22 slope and shape play. Proc. Offshore Technology Conference, Arctic Technology
23 Conference, Houston, USA, May 5-7.

- 1 Barker, A., Timco, G., Gravesen, H., Vølund, P., 2005. Ice loading on Danish wind
2 turbines: part 1: dynamic model tests. *Cold Reg. Sci. Technol.* 41(1), 1–23.
- 3 Bekker, A.T., Sabodash, O.A., SeJiverstov, V., Koff, G., Pipko, E., 2009. Estimation of
4 limit ice loads on engineering offshore structures in the Sea of Okhotsk. *Proc. 19th*
5 *International Offshore and Polar Engineering Conference (ISOPE)*, Osaka, Japan,
6 June 21-26.
- 7 Bekker, A.T., Sabodash, O.A., Balakin, B.V., 2013. Numerical prediction of contact
8 surface between hummock and ice fields for estimation of ice loads on structure.
9 *Proc. 23rd International Offshore and Polar Engineering Conference (ISOPE)*,
10 Alaska, USA, June 30-July 5.
- 11 Bjerkås, M., Alsos, H.S., Wåsjør, K., 2014. Estimates of the number of vibration cycles
12 from frequency locked-in ice loads. *Proc. ASME 2014 33rd International*
13 *Conference on Ocean, Offshore and Arctic Engineering (OMAE)*, San Francisco,
14 USA, June 8-13.
- 15 Bjerkås, M., Meese, A., Alsos, H.S., 2013. Ice induced vibrations-observations of a full
16 scale lock-in event. *Proc. 23rd International Offshore and Polar Engineering*
17 *Conference (ISOPE)*, Alaska, USA, June 30-July 5.
- 18 Corbetta, G., Mbistrova, A., Ho, A., Guillet, J., Pineda, I., 2015. The European offshore
19 wind industry—key trends and statistics 2014. European Wind Energy Association.
- 20 DNV, Det Norske Veritas, 2014. DNV-OS-J101 Offshore Standard: Design of Offshore
21 Wind Turbine Structures.
- 22 Etemaddar, M., Hansen, M.O.L., Moan, T., 2014. Wind turbine aerodynamic response
23 under atmospheric icing conditions. *Wind Energy* 17(2), 241–265.

- 1 Frederking, R., 2012. Comparison of standards for predicting ice forces on arctic
2 offshore structures. Proc. 10th ISOPE Pacific/Asia Offshore Mechanics Symposium,
3 Vladivostok, Russia, October 3–5.
- 4 Gravesen, H., Kärnä, T., 2009. Ice loads for offshore wind turbines in Southern Baltic
5 Sea. Proc. 20th International Conference on Port and Ocean Engineering under
6 Arctic Conditions (POCA'09), Luleå, Sweden, June 9–12.
- 7 Gravesen, H., Petersen, B., Sørensen, S.L., Vølund, P., 2003. Ice forces to wind turbine
8 foundations in Denmark. Proc. 17th International Conference on Port and Ocean
9 Engineering under Arctic conditions (POAC'03), Trondheim, Norway, June 16–19.
- 10 Gravesen, H., Sørensen, S.L., Vølund, P., Barker, A., Timco, G., 2005. Ice loading on
11 Danish wind turbines: Part 2. Analyses of dynamic model test results. Cold Reg. Sci.
12 Technol. 41(1), 25-47.
- 13 Gürtner, A., Bjerkas, M., Kuhnlein, W., Jochmann, P., Konuk, I., 2009. Numerical
14 simulation of ice action to a lighthouse. Proc. 28th International Conference on
15 Ocean, Offshore and Arctic Engineering (OMAE), Hawaii, USA, May31-June5.
- 16 Heinonen, J., Hetmanczyk, S., Strobel, M., 2011. Introduction of ice loads in overall
17 simulation of offshore wind turbines. Proc. 21st International Conference on Port
18 and Ocean Engineering under arctic conditions (POAC'11), Montréal, Canada, July
19 10–14.
- 20 Hendrikse, H., Renting, F.W., Metrikine, A.V., 2014. Analysis of the fatigue life of
21 offshore wind turbine generators under combined ice and aerodynamic loading.
22 Proc. ASME 2014 33rd International Conference on Ocean, Offshore and Arctic
23 Engineering (OMAE), San Francisco, USA, June 8-13.

1 Hetmanczyk, S., Heinonen, J., Strobel, M., 2011. Dynamic ice load model in overall
2 simulation of offshore wind turbines. Proc. 21st International Offshore and Polar
3 Engineering Conference (ISOPE), Maui, USA, June 19–24.

4 Hou, J., Shao, W., 2014. Structural design for the ice-resistant platform. Proc. 24th
5 International Offshore and Polar Engineering Conference (ISOPE), Busan, Korea,
6 June 15-20.

7 IEC 61400-3, 2009. Wind turbines, Part 3: Design requirements for offshore wind
8 turbines, IEC.

9 ISO 19906, 2010. Petroleum and Natural Gas Industries-Arctic Offshore structures.
10 International organization for standardization, ISO 19906, Geneva, Switzerland.

11 Jefferies, M., Rogers, B., Hardy, M., Wright, B., 2011. Ice Load Measurement on
12 Molikpaq: Methodology and Accuracy. Proc. 21st international conference on Port
13 and Ocean Engineering under Arctic Conditions(POAC'11), Montréal, Canada,
14 July 10–14.

15 Jiang, Z.Y., Karimirad, M., Moan, T., 2014. Dynamic response analysis of wind
16 turbines under blade pitch system fault, grid loss, and shutdown events. Wind
17 Energy 17(9), 1385–1409.

18 Jonkman, J., Butterfield, S., Musial, W., Scott, G., 2009. Definition of a 5-MW
19 reference wind turbine for offshore system development. Golden, CO, National
20 Renewable Energy Laboratory. NREL Report TP-500-38060.

21 Jonkman, J., Larsen, T., Hansen, A., Nygaard, T., Maus, K., Karimirad, M., Gao, Z.,
22 Moan, T., Fylling, I., Nichols, J., Kohlmeier, M., Vergara, J.P., Merino, D., Shi, W.,
23 Park, H.C., 2010. Offshore code comparison collaboration within IEA wind task 23:

1 phase IV results regarding floating wind turbine modelling, EWEC2010, Warsaw,
2 Poland.

3 Karimirad, M., Moan, T., 2013. Stochastic dynamic response analysis of a tension leg
4 spar-type offshore wind turbine. *Wind Energy* 16, 953–973.

5 Karna, T., Kolari, K., 2004. Mitigation of dynamic ice actions on offshore wind turbines.
6 Proc. 3rd European Conference on Structural Control, 3ECSC, Vienna, Austria.

7 Larsen, T.J., Hansen, A.M., 2014. How2HAWC2, the User's Manual, Technical Report
8 Risø-R-1597(ver. 4-5) (EN), Risø National Laboratory, 2014.

9 Lu, W., Løset, S., Lubbad, R., 2012. Ventilation and backfill effect during ice–sloping
10 structure interactions. Proc. 21st International Symposium on Ice (IAHR), Dalian,
11 China, pp. 826–841.

12 Määttänen, M., 1999. Ice and offshore wind turbines in the Gulf of Bothnia. Proc. 15th
13 International Conference on Port and Ocean Engineering under Arctic
14 Conditions(POAC 99), Espoo, Finland, August 23-27.

15 Määttänen, M., Marjavaara, P., Saarinen, S., Laakso, M., 2011. Ice crushing tests with
16 variable structural flexibility. *Cold Reg. Sci. Technol.* 67 (3), 120–128.

17 McGovern, D. J. & Bai, W. 2014. Experimental study of wave-driven impact of sea ice
18 floes on a circular cylinder. *Cold Reg. Sci. Technol.* 108, 36-48.

19 Mróz, A., Holnicki-Szulc, J., Kärnä, T., 2008. Mitigation of ice loading on offshore
20 wind turbines: Feasibility study of a semi-active solution. *Comput. Struct.* 86(3),
21 217–226.

22 Murray, J., LeGuennec, S., Spencer, D., Yang, C.K., Yang, W., 2009. Model tests on a
23 spar in level ice and ice ridge conditions. Proc. 28th International conference on
24 Ocean, Offshore and Arctic Engineering (OMAE), Hawaii, USA, May31-June5.

1 Nguyen, N.C., Meyer, C., Gujer, P., 2014. Deterministic and Stochastic Approach to
2 Consider Dynamic Sea Ice Loads in GL/IEC/ISO Standards. European Wind
3 Energy Conference & Exhibition 2014, Barcelona, Spain, March 10–13.

4 Nord, T.S., Lourens, E.M., Øiseth, O., Metrikine, A., 2015. Model-based force and state
5 estimation in experimental ice-induced vibrations by means of Kalman filtering.
6 Cold Reg. Sci. Technol. 111, 13–26.

7 Perveen, R., Kishor, N., Mohanty, S.R., 2014. Offshore wind farm development:
8 Present status and challenges. *Renew. Sust. Energy Rev.* 29, 780–792.

9 Popko, W., Heinonen, J., Hetmanczyk, S., Vorpahl, F., 2012a. State-of-the-art
10 comparison of standards in terms of dominant sea ice loads for offshore wind
11 turbine support structures in the Baltic Sea. Proc. 22nd International Offshore and
12 Polar Engineering Conference (ISOPE), Rhodes, Greece, June 17–22.

13 Popko, W., Vorpahl, F., Zuga, A., Kohlmeier, M., Jonkman, J., Robertson, A., Larsen,
14 T.J., Yde, A., Sætertrø, K., Okstad, K.M., Nichols, J., Nygaard, T.A., Gao, Z.,
15 Manolas, D., Kim, K., Yu, Q., Shi, W., Park, H., Vásquez-Rojas, A., Dubois, J.,
16 Kaufer, D., Thomassen, P., de Ruyter, M.J., Peeringa, J.M., Huang, Z.W., von
17 Waaden, H., 2012b. Offshore code comparison collaboration continuation (OC4),
18 phase I - results of coupled simulations of an offshore wind turbine with jacket
19 support structure. Proc. 22nd International Offshore and Polar Engineering
20 Conference (ISOPE), Rhodes, Greece, June 17–22.

21 Ralston, T.D., 1977. Ice force design considerations for conical offshore structures.
22 Proc. 4th International Conference on Port and Ocean Engineering under Arctic
23 Conditions(POAC 77), Newfoundland, Canada, September 26–30.

1 Riska, K., 1995. Models of ice–structure contact for engineering applications.
2 Mechanics of Geomaterial Interfaces 42, 77–103.

3 Robertson, A. et al., 2014. Offshore Code Comparison Collaboration Continuation
4 Within IEA Wind Task 30: Phase II Results Regarding a Floating
5 Semisubmersible Wind System. National Renewable Energy Laboratory, Golden,
6 CO, Technical Report No. NREL/CP-5000-61154.

7 Ronsten, G., Wallenius, T., Hulkkonen, M., Baring-Gould, I., Cattin R., Durstewitz, M.,
8 Krenn, A., Laakso, T., Lacroix, A., Tallhaug, L., Byrkjedal, Ø., Peltola, E., 2012. State-
9 of-the-art of wind energy in cold climates. IEA R&D Wind, Wind Energy in Cold
10 Climates, October 2012.

11 Salo, O., Syri, S., 2014. What economic support is needed for Arctic offshore wind
12 power? Renew. Sust. Energy Rev. 31, 343-352.

13 Shi, W., Park, H.C., Han, J.H., Na, S.K., Kim, C.W., 2013. A study on the effect of
14 different modeling parameters on the dynamic response of a jacket-type offshore
15 wind turbine in the Korean Southwest Sea. Renewable Energy 58, 50–59.

16 Shi, W., Tan, X., Gao, Z., Moan, T., 2014. Study on the effect of ice-structure
17 interaction on the dynamic response of offshore wind turbine. Proc. 1st International
18 Conference on Renewable Energies Offshore (RENEW2014), Lisbon, Portugal,
19 November 24-26.

20 Spencer, P., Morrison, T., Ausenco, C., 2014. Quantile regression as a tool for
21 investigating local and global ice pressures. Proc. Offshore Technology Conference,
22 Arctic Technology Conference Houston, USA, May 5-7.

23 Su, B., Riska, K., Moan, T., 2010. A numerical method for the prediction of ship
24 performance in level ice. Cold Reg. Sci. Technol. 60, 177–188.

1 Tan, X., Su, B., Riska, K., Moan, T., 2013. A six-degrees-of-freedom numerical model
2 for level ice–ship interaction. *Cold Reg. Sci. Technol.* 92, 1–16.

3 Tan, X., Riska, K., Moan, T., 2014. Effect of Dynamic Bending of Level Ice on Ship's
4 Continuous-Mode Icebreaking. *Cold Reg. Sci. Technol.* 106–107, 82–95.

5 Taylor, R. S., Richard, M., 2014. Development of a probabilistic ice load model based
6 on empirical descriptions of high pressure zone attributes. *Proc. ASME 2014 33rd*
7 *International Conference on Ocean, Offshore and Arctic Engineering (OMAE)*, San
8 Francisco, USA, June 8-13.

9 Tuomi, L., Kahma, K. K., Pettersson, H., 2011. Wave hindcast statistics in the
10 seasonally ice-covered Baltic Sea. *Boreal environment research*, 16(6), 451-472.

11 Xu, N., Yue, Q.J., 2014. Dynamic Ice Force Analysis on a Conical Structure Based on
12 Direct Observation and Measurement. *J. Offshore Mech. Arct. Eng.* 136(1), 014501.

13 Xu, N., Yue, Q., Qu, Y., Yuan, S., Liu, X., 2014. Comparison and cause analysis of ice-
14 induced structural vibration of upward and downward cones. *Proc. 24th*
15 *International Offshore and Polar Engineering Conference (ISOPE)*, Busan, Korea,
16 June 15-20.

17 Yu, B., Karr, D.G., Song, H., Srinivas, S., 2013. A surface ice module for wind turbine
18 dynamic response simulation using FAST. *Proc. 32nd International Conference on*
19 *Ocean, Offshore and Arctic Engineering (OMAE)*, Nantes, France, June 9–14.

20 Yu, B., Karr, D. G., Srinivas, S., 2014. Ice nonsimultaneous failure, bending and floe
21 impact modelling for simulating wind turbine dynamics using FAST. *Proc. ASME*
22 *2014 33rd International Conference on Ocean, Offshore and Arctic Engineering*
23 *(OMAE)*, San Francisco, USA, June 8-13.

- 1 Yue, Q.J., Guo, F., Kärnä, T., 2009. Dynamic ice forces of slender vertical structures
2 due to ice crushing. *Cold Reg. Sci. Technol.* 56(2), 77–83.
- 3 Zhou, L., Riska, K., und Polach, R.V.B., Moan, T., Su, B., 2013. Experiments on level
4 ice loading on an icebreaking tanker with different ice drift angles. *Cold Reg. Sci.*
5 *Technol.* 85, 79-93.
- 6 Zvyagin, P., Sazonov, K. 2014. Analysis and probabilistic modelling of the stationary
7 ice loads stochastic process with lognormal distribution. *Proc. ASME 2014 33rd*
8 *International Conference on Ocean, Offshore and Arctic Engineering*, San
9 Francisco, USA, June 8-13.

Figure Captions

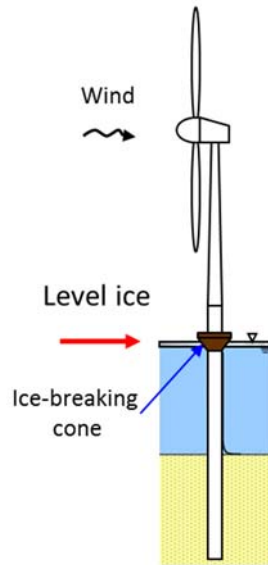


Fig. 1. Monopile wind turbine with ice-breaking cone.

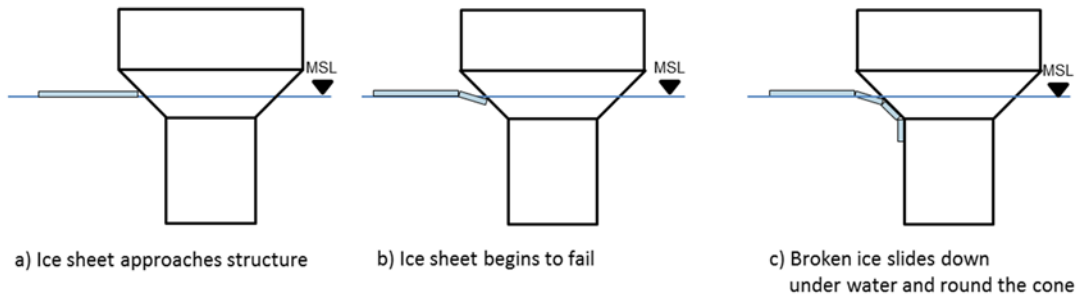


Fig. 2. Interaction between a sloping structure and level ice (reproduced from ISO (2010)).

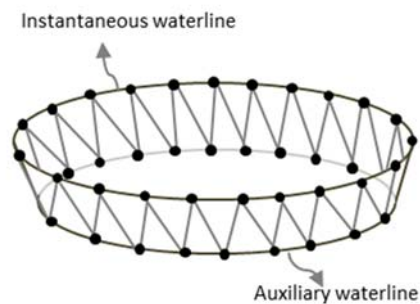
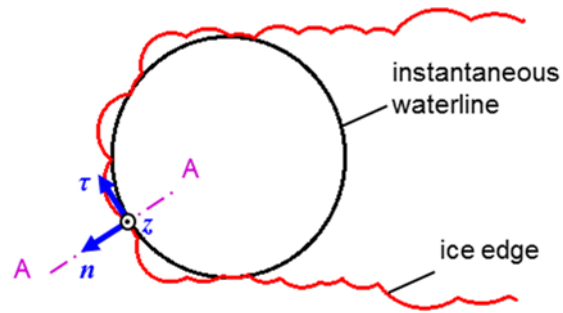
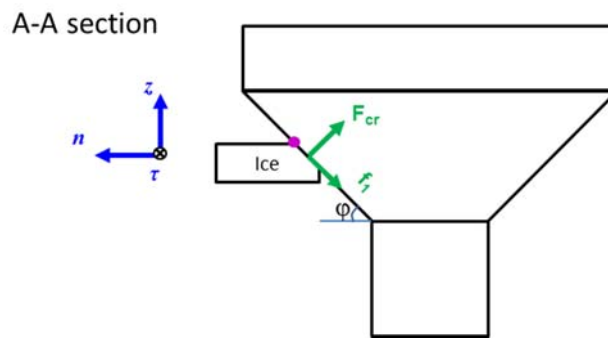


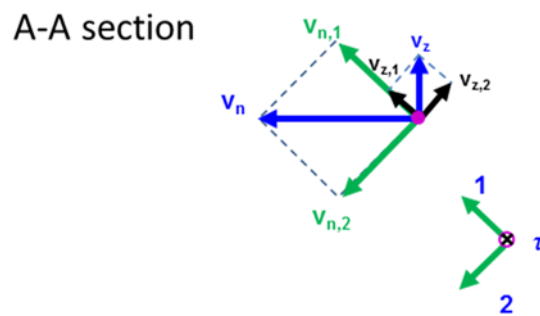
Fig. 3. Modeling of the structural geometry at the MSL.



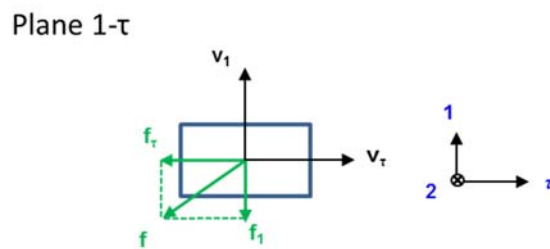
(a)



(b)



(c)



(d)

Fig. 4. (a) Local contact zone and coordinate system. (b) Contact force on the structure on n - z plane. (c) Velocity decomposition on A-A section. (d) Local contact forces on the structure on l - τ plane (reproduced from (Tan et al., 2014)).

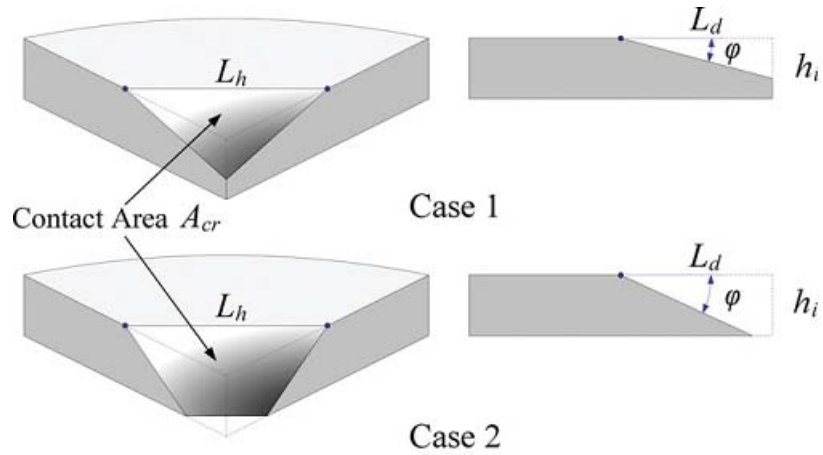


Fig. 5. Two cases of ice contact geometry (Su et al., 2010).

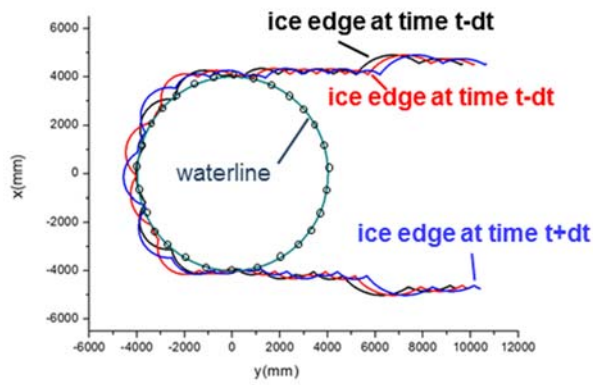


Fig. 6. Example of ice-breaking pattern.

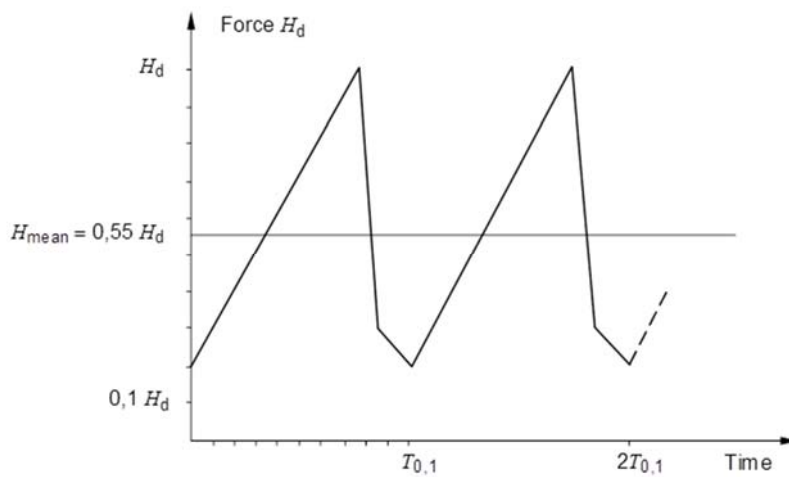


Fig. 7. IEC sawtooth ice load model (IEC 61400-3, 2009).

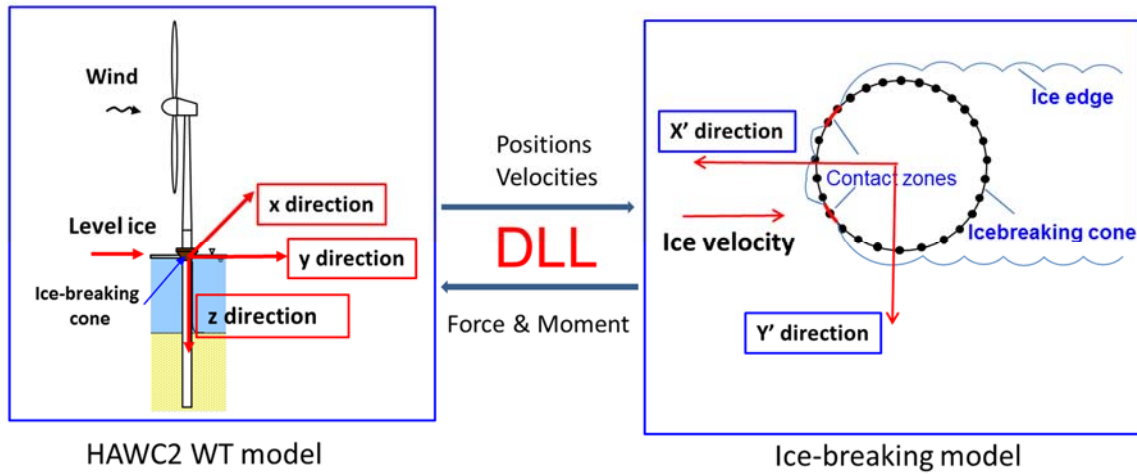


Fig. 8. Coupling between the HAWC2 WT model and the ice-breaking model.

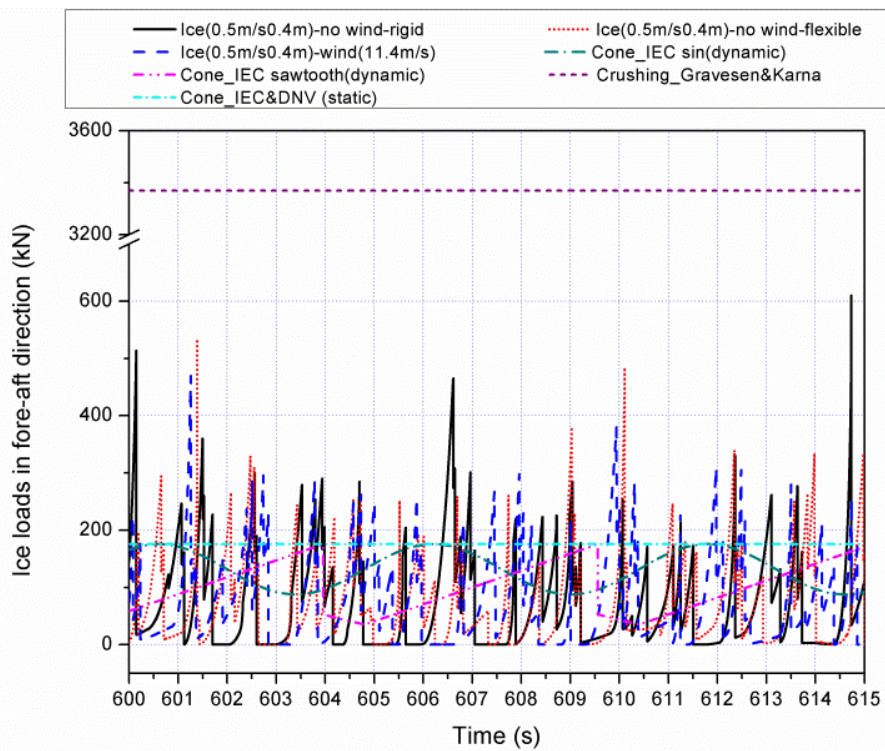


Fig. 9. Time series of the ice loads in the F-A direction at the MSL. $h_i = 0.4$ m, $V_i = 0.5$ m/s, $V_{wind} = 11.4$ m/s, $D_{wl} = 8$ m.

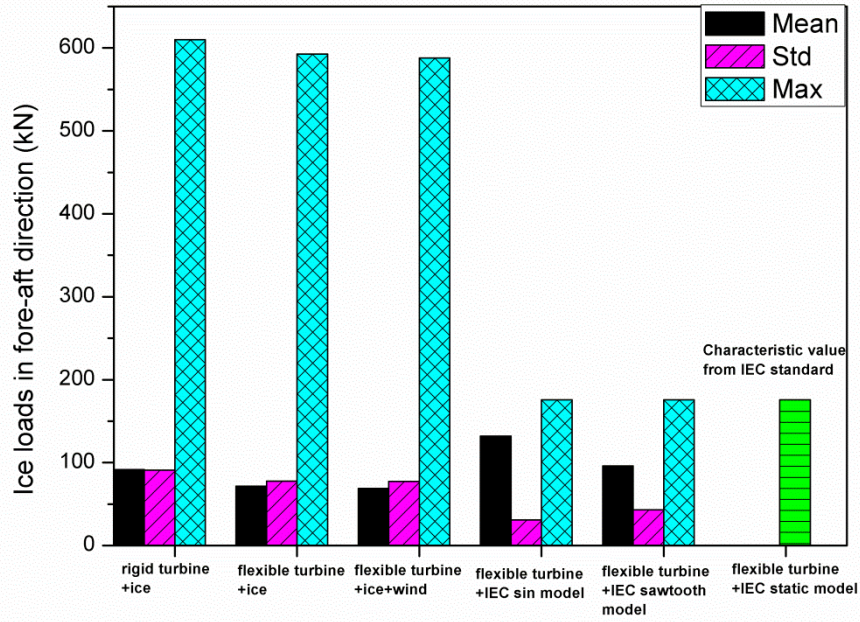


Fig. 10. Statistical properties of the ice loads shown in Fig. 9. $h_i = 0.4$ m, $V_i = 0.5$ m/s, $V_{wind} = 11.4$ m/s, $D_{wl} = 8$ m.

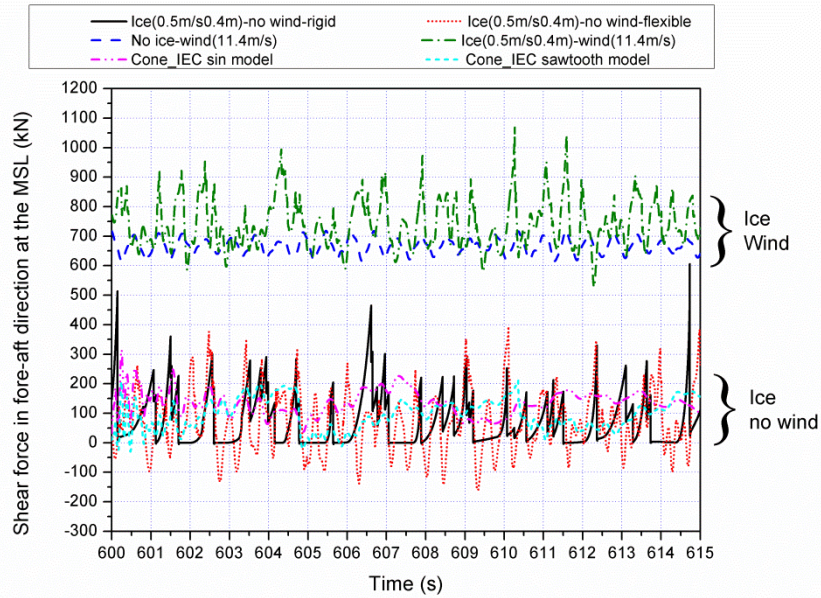


Fig. 11. Time series of the shear force response in F-A direction at the MSL. $h_i = 0.4$ m, $V_i = 0.5$ m/s, $V_{wind} = 11.4$ m/s, $D_{wl} = 8$ m.

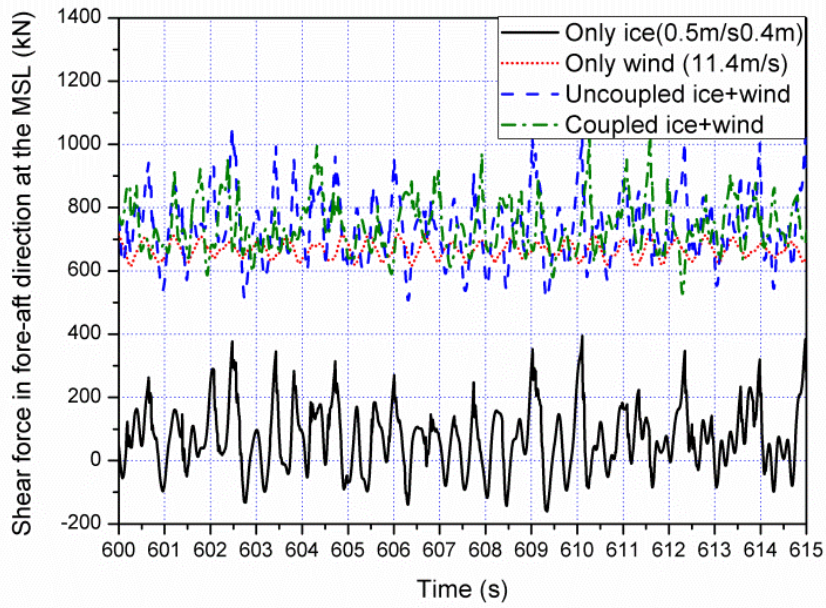
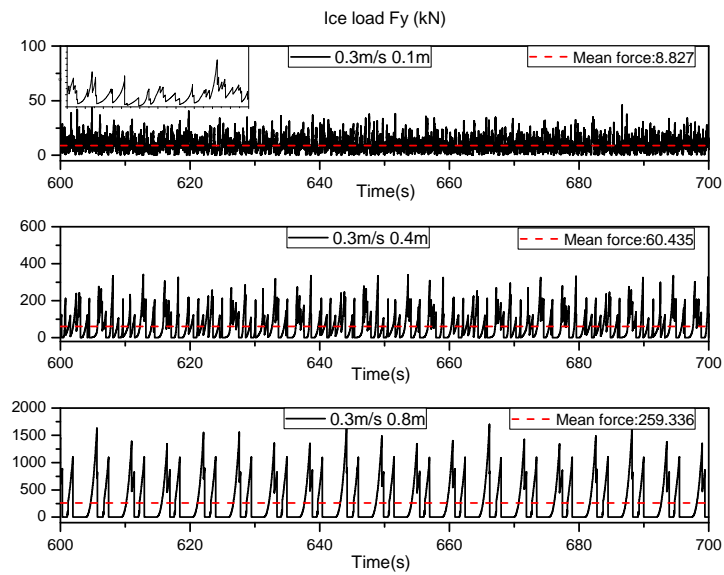


Fig. 12. Comparison of the shear force in F-A direction at the MSL under various load conditions. $h_i = 0.4$ m, $V_i = 0.5$ m/s, $V_{wind} = 11.4$ m/s, $D_{wl} = 8$ m.



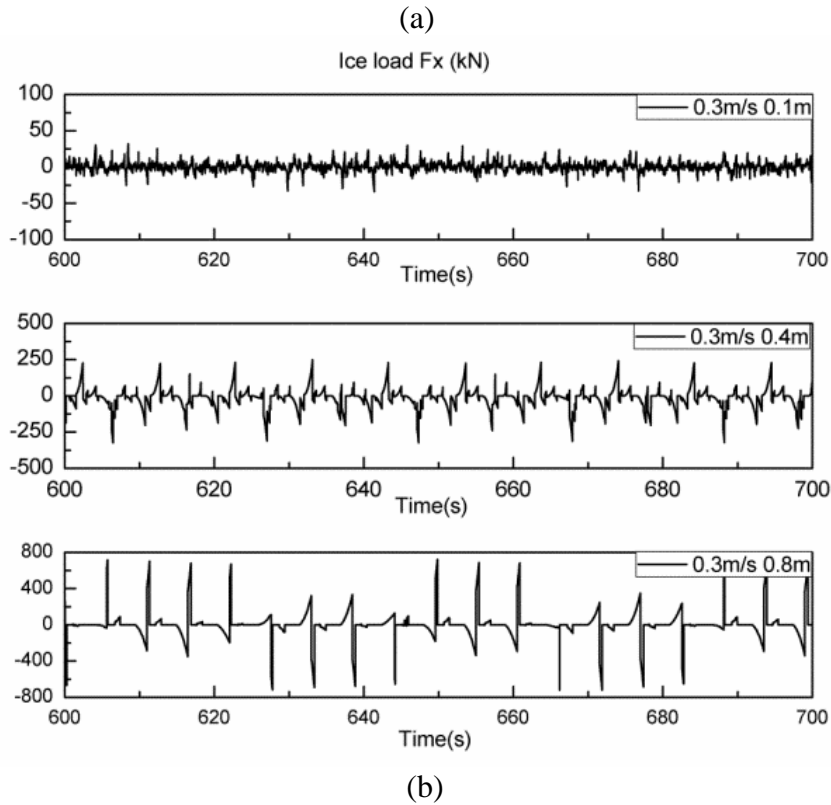
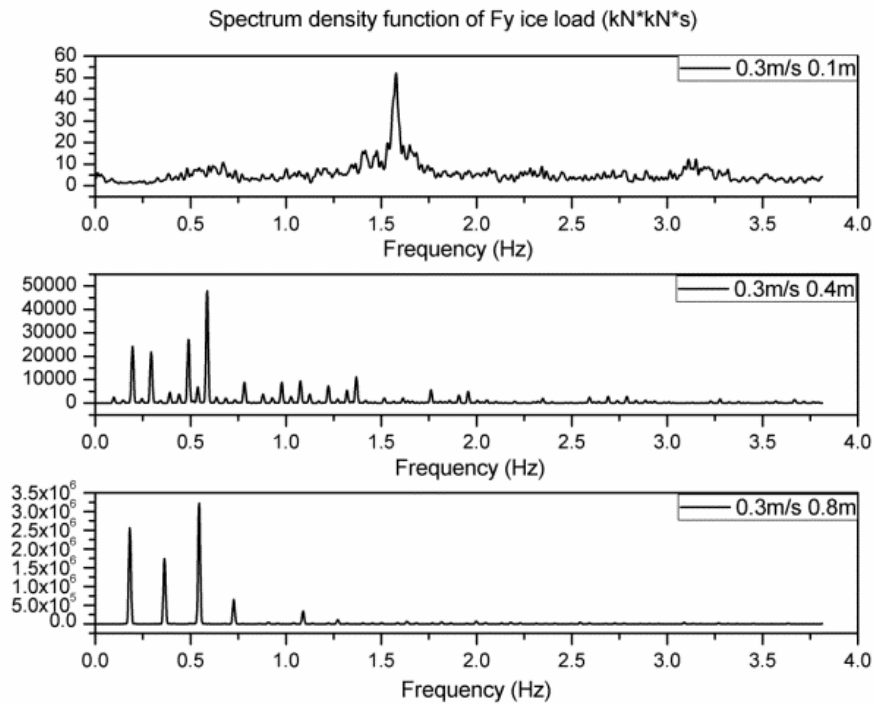
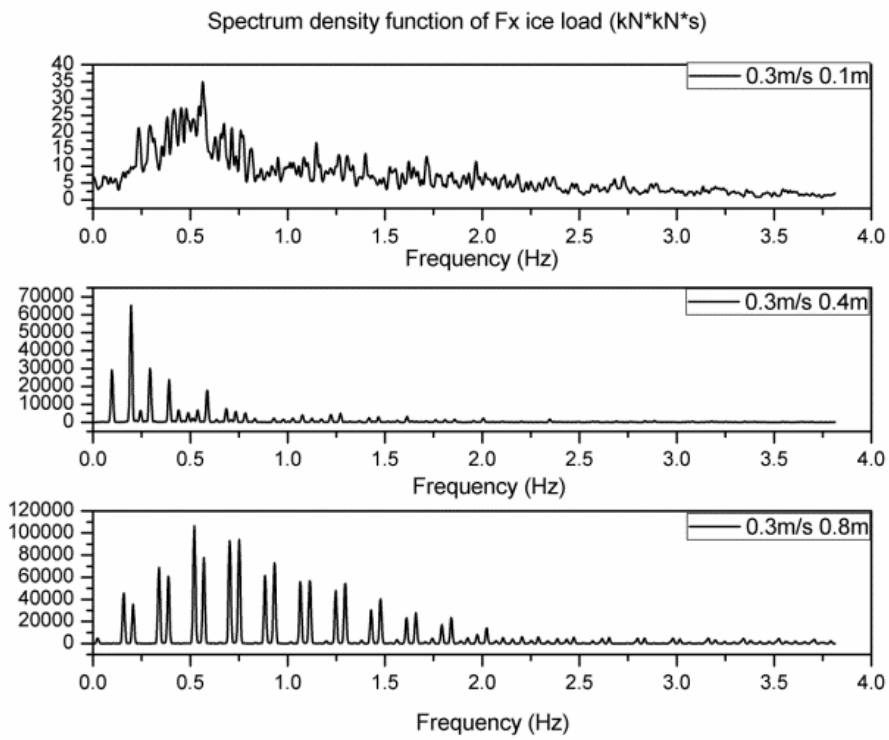


Fig. 13. Time series of the simulated ice load at the MSL with different ice thicknesses:

(a) ice load in the F-A direction, (b) ice load in the S-S direction. $V_i = 0.3$ m/s.



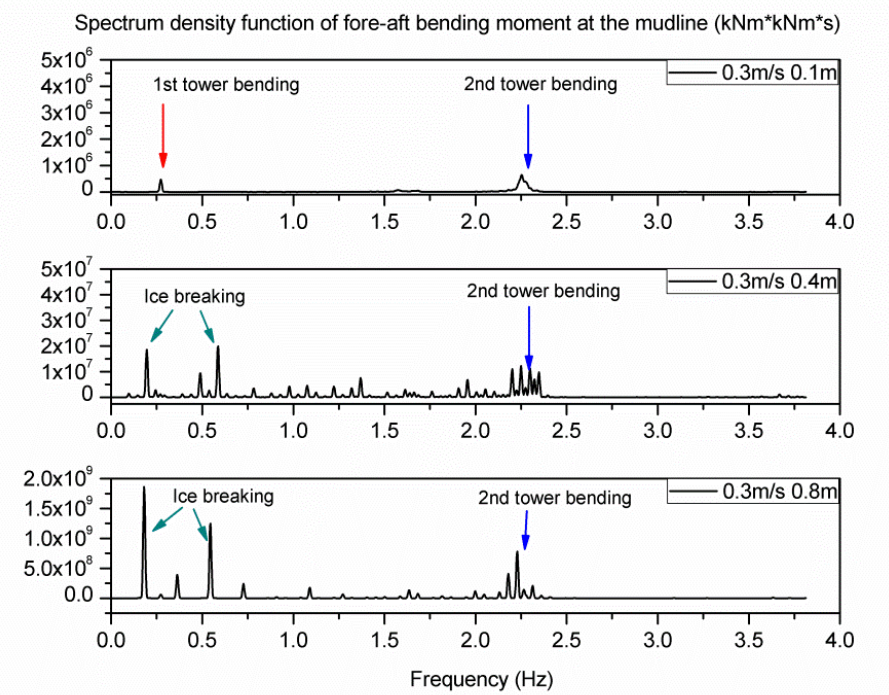
(a)



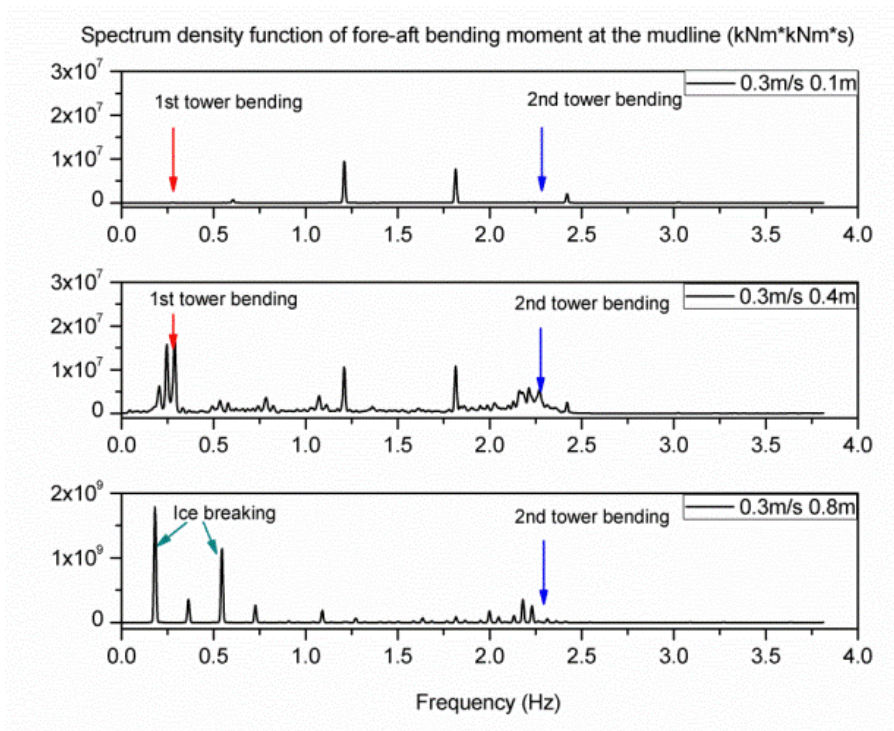
(b)

Fig. 14. Spectra of the simulated ice load at the MSL with different ice thicknesses: (a)

ice load in the F-A direction, (b) ice load in the S-S direction. $V_i = 0.3$ m/s.

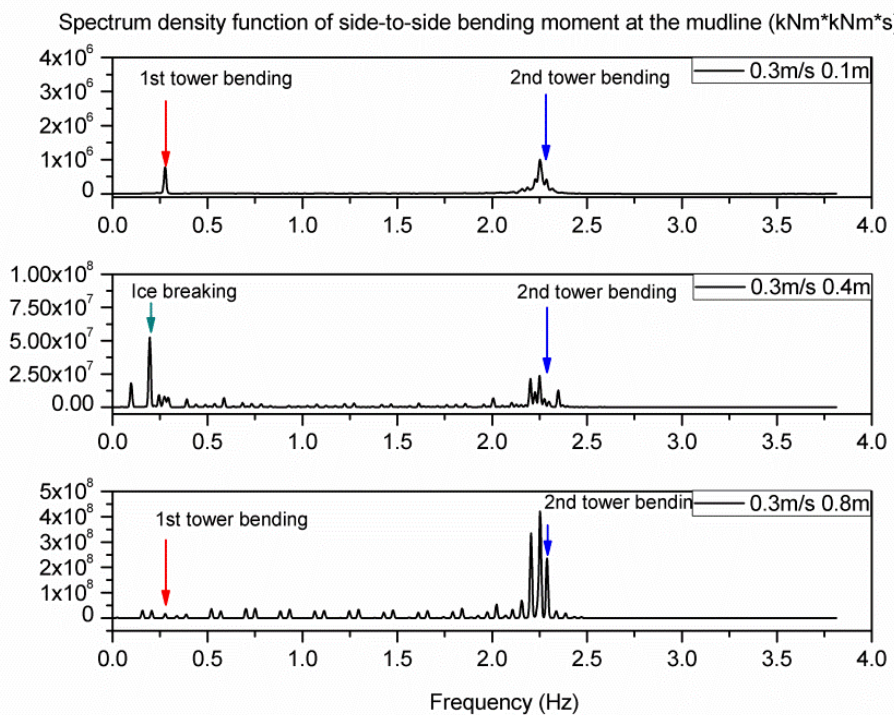


(a)

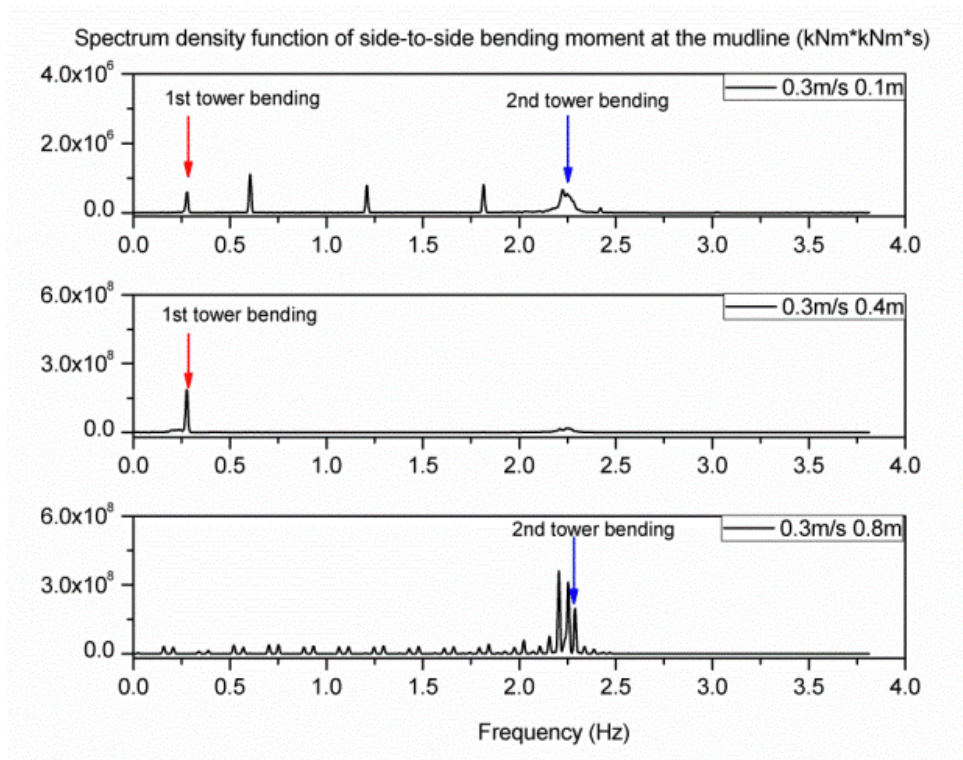


(b)

Fig. 15. Spectra of the wind turbine F-A bending moment at the mudline with different ice thicknesses under parked and operating conditions: (a) wind speed=0 m/s; (b) wind speed=18 m/s. $V_i = 0.3$ m/s.

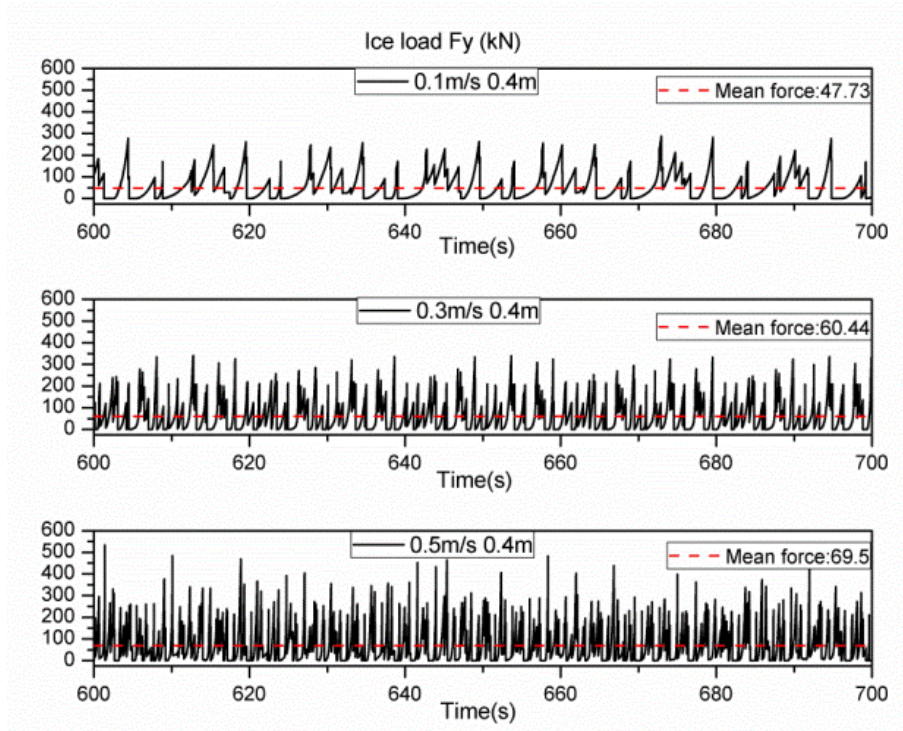


(a)

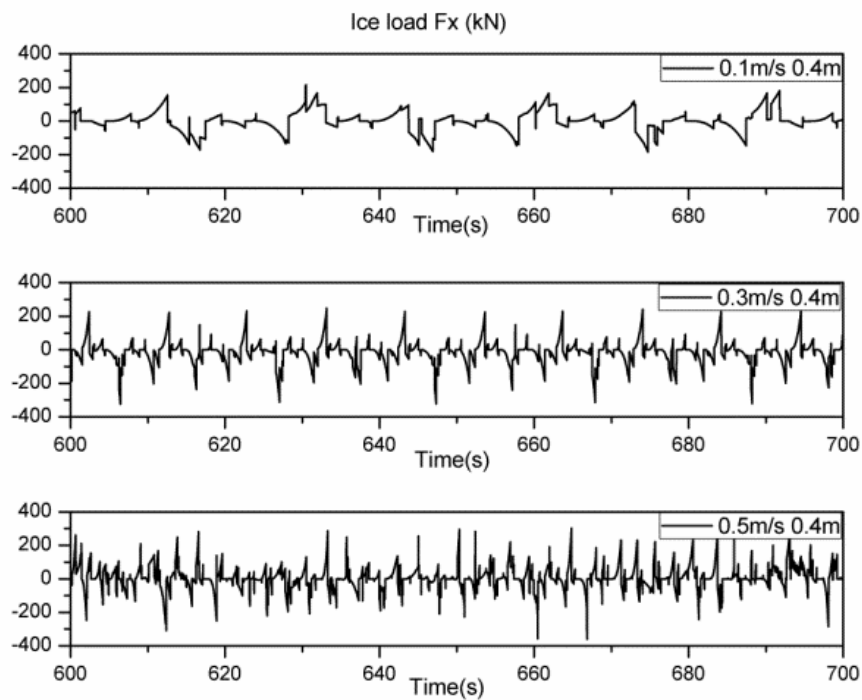


(b)

Fig. 16. Spectra of the wind turbine S-S bending moment at the mudline with different ice thicknesses under parked and operating conditions: (a) wind speed=0 m/s; (b) wind speed=18 m/s. $V_i = 0.3$ m/s.

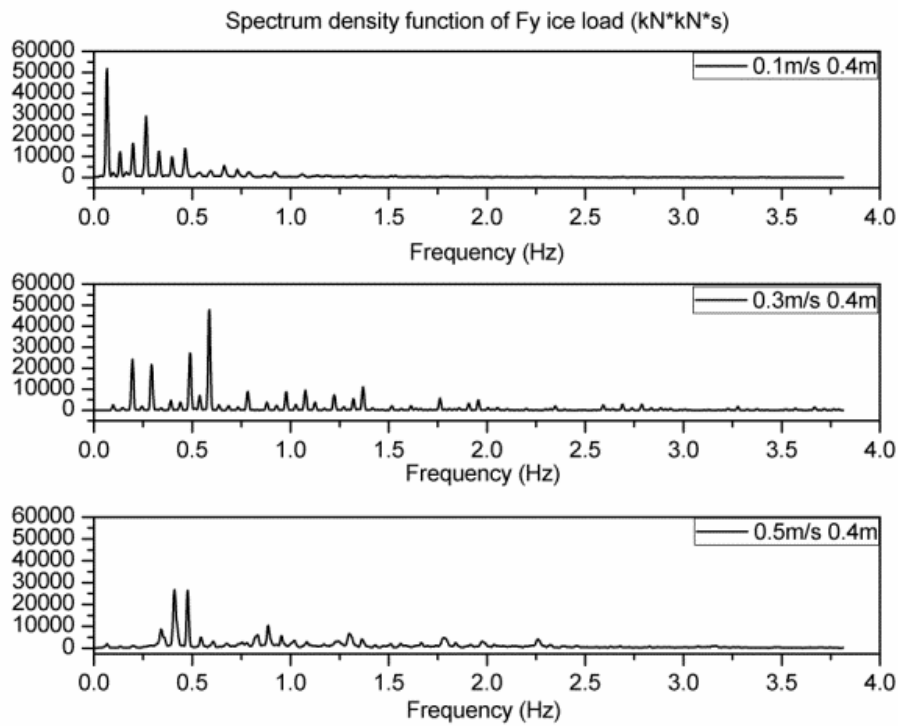


(a)

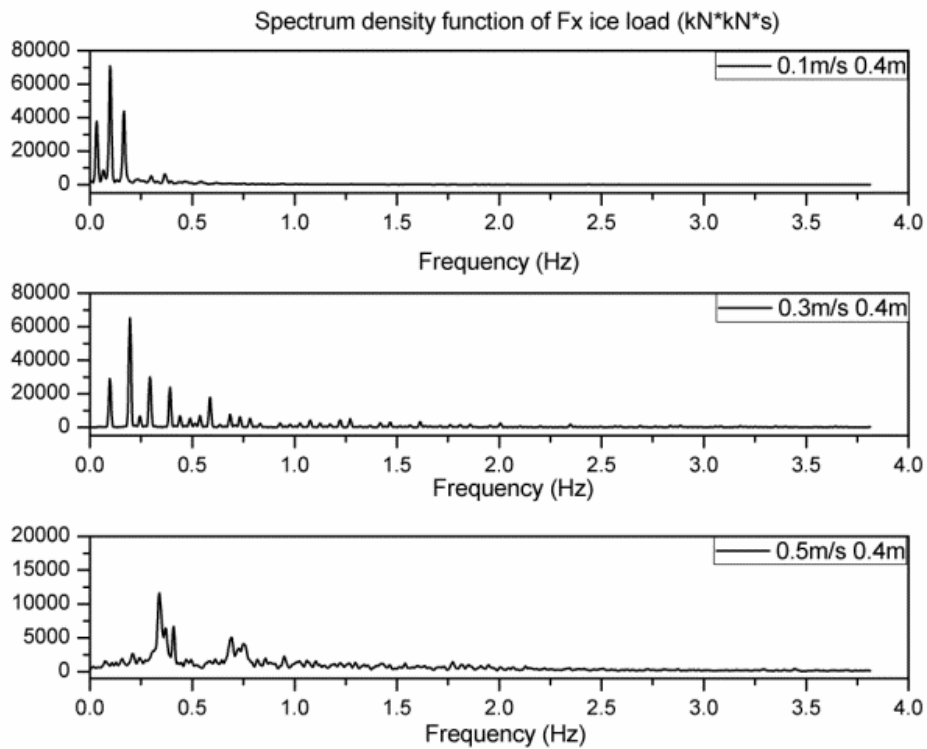


(b)

Fig. 17. Time series of the simulated ice load at the MSL with different ice drifting speeds: (a) ice load in the F-A direction; (b) ice load in the S-S direction. $h_i = 0.4$ m.



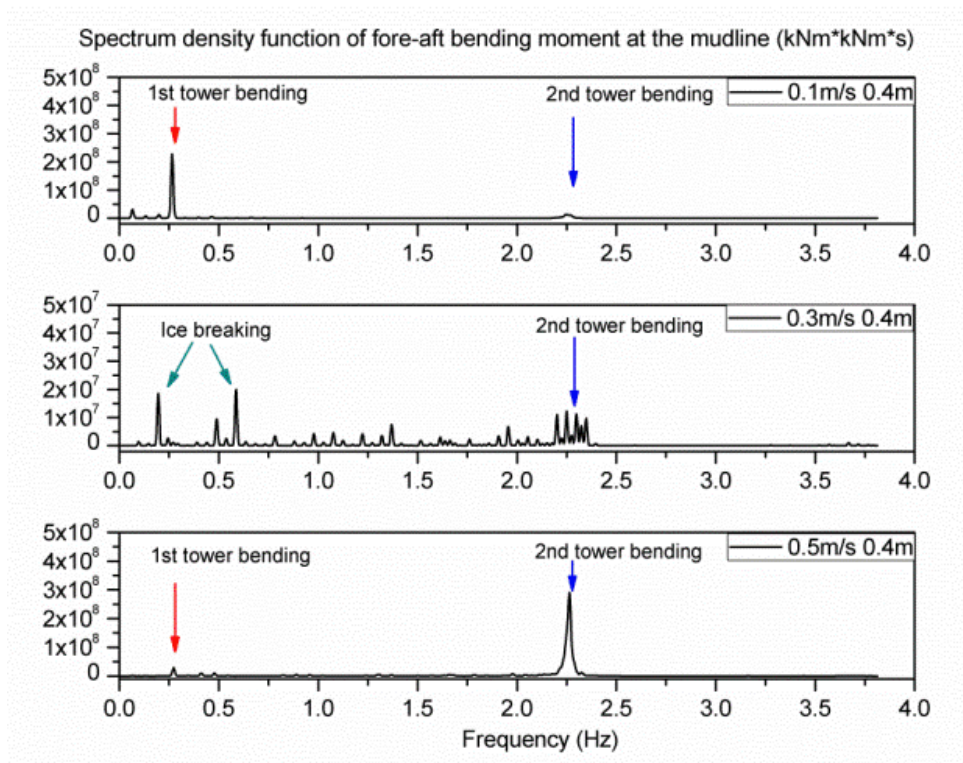
(a)



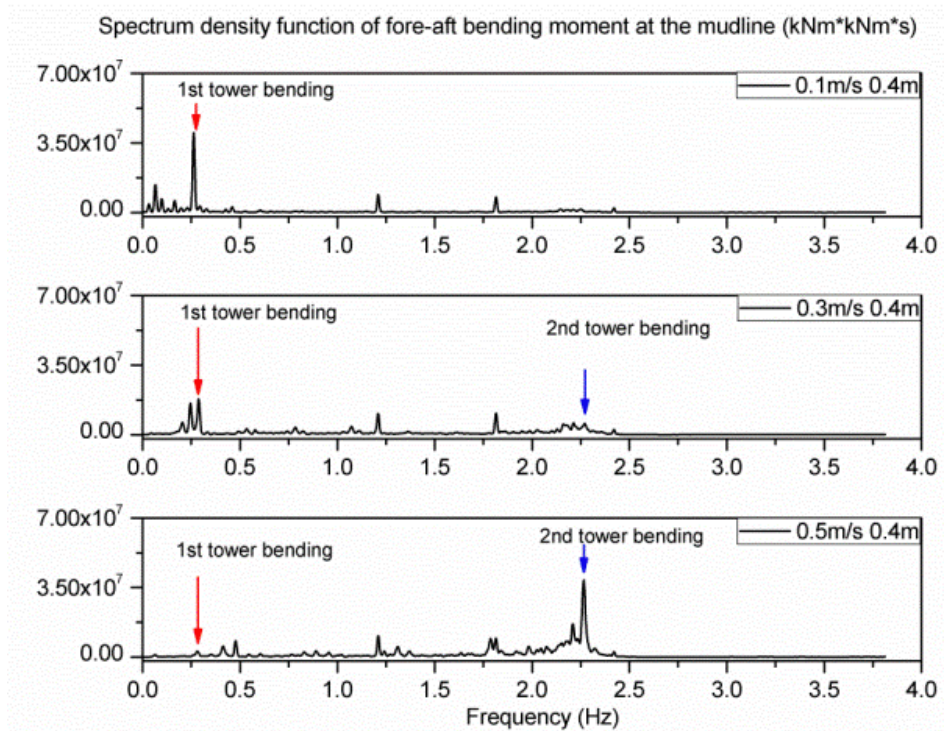
(b)

Fig. 18. Spectra of the simulated ice load at the MSL with different ice drifting speeds:

(a) ice load in the F-A direction; (b) ice load in the S-S direction. $h_i = 0.4$ m.

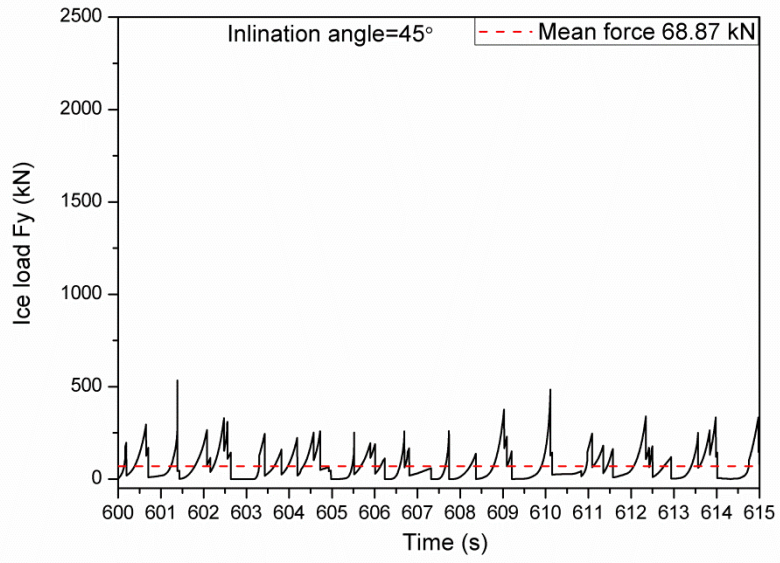


(a)

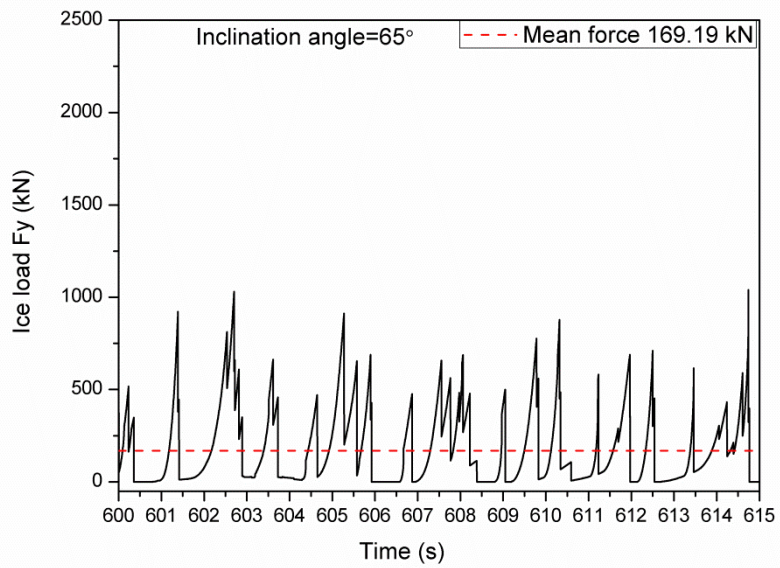


(b)

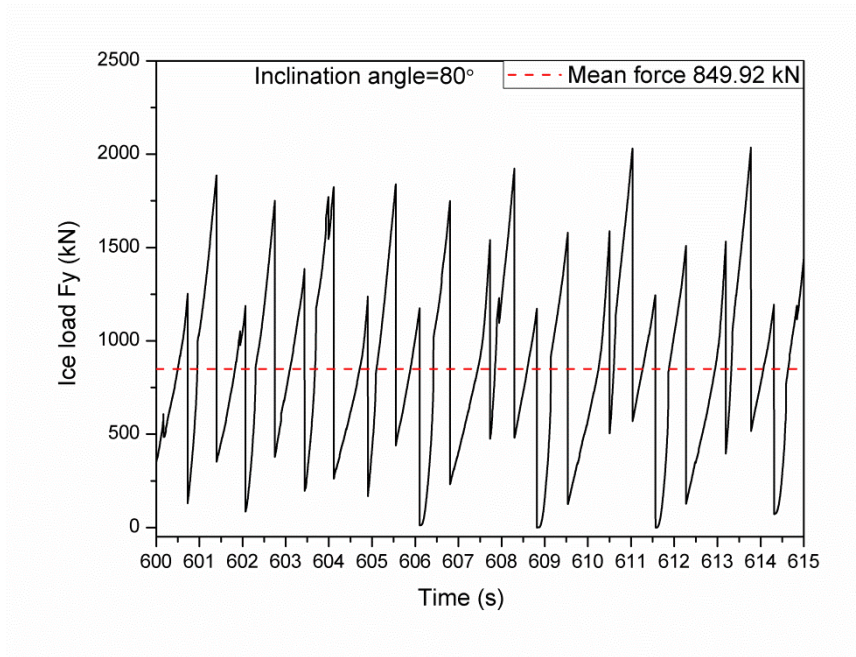
Fig. 19. Spectra of the wind turbine F-A bending moment at the mudline with different ice drifting speeds: (a) wind speed=0 m/s; (b) wind speed=18 m/s. $h_i = 0.4$ m.



(a)



(b)



(c)

Fig. 20. Time series of the simulated ice load in the F-A direction at the MSL with different inclination angles of the cone. $h_i = 0.4$ m, $V_i = 0.5$ m/s, $V_{wind} = 0$ m/s, $D_{wl} = 8$ m.